J. Fluid Mech. (2020), *vol.* 883, A23. © Cambridge University Press 2019 **883** A23-1
doi:10.1017/jfm.2019.856

Real-fluid effects on standing-wave thermoacoustic instability

Mario Tindaro Migliorino[1,†] **and Carlo Scalo**[1]

[1]Department of Mechanical Engineering, Purdue University, West Lafayette, IN 47907, USA

(Received 12 March 2019; revised 9 October 2019; accepted 17 October 2019)

We have performed high-order compressible Navier–Stokes simulations of a thermoacoustically unstable resonator employing CO_2 in transcritical conditions. The parameter space spans the range of base pressures $p_0 = 1.01 - 1.5\,p_{cr}$ and temperature differences $\Delta T = T_{hot} - T_{cold}$ up to 200 K, with thermodynamic and transport properties obtained from the Peng–Robinson equation of state and Chung's model. The set-up is a classic standing-wave thermoacoustic resonator, which has been optimized resulting in a minimum temperature difference required to sustain the instability of 23 K. Strong real-fluid effects in the thermoacoustic response in the linear regime are observed: (i) the thermoviscous functions need to depend on the complex eigenvalue (and not just the angular frequency) for linear theory to accurately predict the growth rate observed in the Navier–Stokes simulations, due to a high growth-rate-to-frequency ratio; (ii) the growth rate and frequency vary in a non-monotonic fashion with respect to p_0 and ΔT; (iii) the pressure eigenmode amplitude tends to flatten out, and the pressure–velocity phase difference smoothly transitions from $\pi/2$ to $-\pi/2$ at the average pressure node location; and (iv) the sharp change in base acoustic impedance at transcritical conditions introduces a discontinuity in the eigenmodes' spatial derivative. The energy budgets illustrate, for a given ΔT, the increase of the acoustic power produced, but also of the heat input required, for thermodynamic conditions approaching the critical point. Finally, intense mass transport events at transcritical conditions are shown to entail thermodynamic and convective nonlinearities, which do not, however, govern the limit cycle physics, dominated instead by nonlinear minor losses.

Key words: gas dynamics, acoustics, Navier–Stokes equations

1. Introduction

Fluid dynamic instabilities featuring acoustic wave amplification due to the two-way coupling between pressure and heat release fluctuations (Rayleigh 1878) are known as thermoacoustic instabilities. These are intentionally triggered in thermoacoustic engines (TAE) (Swift 1988), where an external temperature differential imposed on a compact region of the device (thermoacoustic stack or regenerator) results in the

† Present address: Department of Mechanical and Aerospace Engineering, Sapienza University of Rome, 00184 Rome, Italy. Email address for correspondence: mariotindaro.migliorino@uniroma1.it

spontaneous generation of acoustic power. Thermoacoustic engines have received much attention from the worldwide community (Ceperley 1979; Migliori & Swift 1988; Yazaki *et al.* 1998; Backhaus & Swift 1999, 2000; Tijani & Spoelstra 2011) due to the very high energy conversion efficiency potential associated with the quasi-isentropic nature of wave energy propagation and the absence of moving parts. Thermoacoustic engines applications span from NASA designs for deep-space energy generation (Petach, Tward & Backhaus 2004) to small-scale CPU-generated heat control, patented by Google (Elison, Mann & Sinha 2014).

The mechanisms driving thermoacoustic instabilities in TAE rely on a Brayton-like thermodynamic cycle occurring inside the thermoacoustic stack (Swift 1988), comprising two near-adiabatic transformations, driven by the acoustics, and two near-isobaric irreversible heat transfer transformations, which combined cause a fluid particle to experience thermal expansion/contraction at a high/low pressure, powering the instability and spontaneously converting heat into acoustic power. The operating fluid and the base state conditions, hereinafter indicated by a subscript 0, play a fundamental role during the heat-exchange phases of the cycle. Indeed, the theoretical thermoacoustic production is proportional to the thermoacoustic gain, defined by Swift (1988) as

$$\Theta = -\frac{1}{\rho_0}\frac{\mathrm{d}\rho_0}{\mathrm{d}x}, \tag{1.1}$$

where x indicates the coordinate of wave propagation and ρ_0 is the base density. If the base pressure p_0 is uniform, equation (1.1) reverts to

$$\Theta = \alpha_{p_0}\frac{\mathrm{d}T_0}{\mathrm{d}x}, \tag{1.2}$$

where T_0 is the base temperature and

$$\alpha_p = -\frac{1}{\rho}\left.\frac{\partial\rho}{\partial T}\right|_p \tag{1.3}$$

is the isobaric thermal expansion coefficient, which is simply equal to $1/T$ for perfect ideal gases.

Fluids in thermodynamic conditions close to their critical point are characterized by large thermal expansion coefficients, and their use would, theoretically, greatly increase the thermoacoustic gain in (1.2). In particular, for fluids in transcritical, or pseudo-boiling (PB) conditions (Fisher & Widom 1969; Tucker 1999; Banuti 2015), wave-induced compressions and dilatations could be so large that periodic transitions from liquid-like fluid (pseudo-liquid) to gas-like fluid (or pseudo-gas) would occur (see figures 1 and 2). Around the PB region, the highly nonlinear coupling between pressure, temperature and density (thermodynamic nonlinearity) has been proposed by Herring & Heister (2006) as the reason for undesired effects such as thermoacoustic instabilities in high-pressure combustion chambers (Casiano, Hulka & Yang 2010; Poinsot & Veynante 2011) or bulk-mode oscillations in pressurized fuel heat exchangers (Hines & Wolf 1962; Faith, Ackerman & Henderson 1971; Linne *et al.* 1997; Hitch & Karpuk 1998; Herring 2007; Palumbo 2009; Hunt & Heister 2014; Wang *et al.* 2015; Hunt 2016), often leading to catastrophic hardware failure. These phenomena are similar to the multiphase instabilities called density wave oscillations (O'Neill & Mudawar 2018). The regions of the phase space considered in the literature are shown in figure 1.

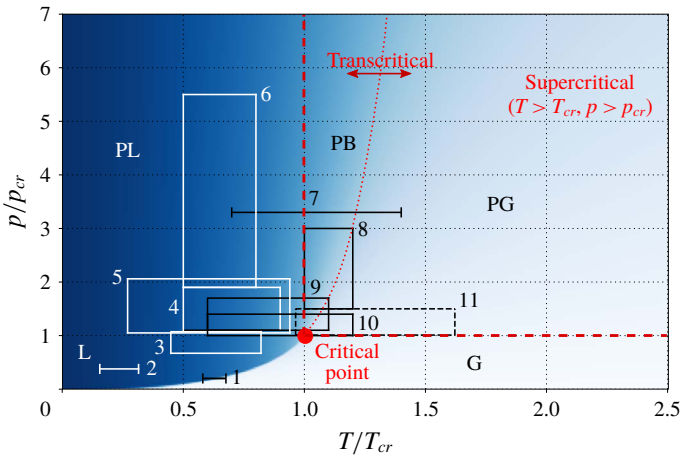

Number	Reference	Fluid	Notes
1	O'Neill & Mudawar (2018)	FC-72	Two-phase flow
2	Migliori & Swift (1988)	Sodium	Liquid, subcritical pressure
3	Wang *et al.* (2015)	RP-3	In between L and PL conditions
4	Herring (2007)	JP-10	PL conditions
5	Hunt (2016)	Jet-A	PL conditions
6	Hines & Wolf (1962)	DECH and RP-1	PL conditions, high pressures
7	Linne *et al.* (1997)	JP-7	Transcritical, high pressures
8	Faith *et al.* (1971)	Jet-A	Transcritical
9	Hitch & Karpuk (1998)	MCH and JP-7	Transcritical
10	Palumbo (2009)	Methanol	Transcritical
11	Current work	CO_2	Transcritical

FIGURE 1. Generic state diagram showing the range of thermodynamic conditions with respect to the critical point ($T = T_{cr}$, $p = p_{cr}$) considered in previous studies of thermoacoustic instabilities involving either multiphase mixtures, liquids or supercritical fluids. The abbreviations L, PL, PB, PG and G stand for fluid in liquid, pseudo-liquid, pseudo-boiling, pseudo-gaseous and gaseous conditions, respectively.

The use of a fluid close to its critical point in a thermoacoustic engine was already suggested by Swift (1988). In fact, the power energy density is proportional to $\alpha_{p_0} T_0$, making a high thermal expansion coefficient one of the basic requirements in the selection of the working fluid. However, the high pressures involved in the handling of transcritical fluids, together with the drop of their thermal diffusivity (hence requiring very small pore size in the heat exchangers and stack), has limited their use in a thermoacoustic engine so far (Alexander *et al.* 2018). Moreover, high-fidelity numerical simulations of transcritical thermoacoustic instabilities have not been carried out yet. One of the major challenges is the use of fully conservative schemes (Karni 1994; Abgrall 1996; Toro 2002), for which spurious numerical oscillations have been shown to produce unstable computations when transcritical flows are considered (Kawai, Terashima & Negishi 2015; Pantano, Saurel & Schmitt 2017; Migliorino *et al.* 2018). The most relevant previous work is the development of the linear thermoacoustic theory, applicable to a generic fluid, by Swift (1988), which builds

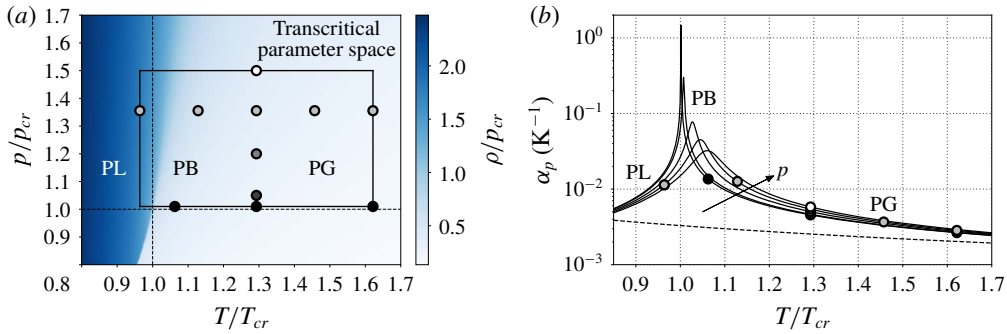

FIGURE 2. (*a*) Flooded contours of reduced density for CO_2; (*b*) isobaric thermal expansion coefficient (1.3) versus reduced temperature for CO_2 at the pressures indicated in table 2. The rectangle drawn in (*a*) shows the parameter space of the linear stability analysis, while the 11 configurations of T_{hot} and p_0 for the Navier–Stokes computations are indicated with circles. The curves in (*b*) are obtained with the PR EoS (solid lines) and with the perfect ideal gas EoS (dashed line, $1/T$).

upon classical linear theory (Kirchhoff 1868; Kramers 1949; Rott 1969). This theory was applied to the design of a thermoacoustic engine successfully operated with liquid sodium (Migliori & Swift 1988), which demonstrated that fluids other than ideal gases, and in particular liquids, which had been employed before in Malone-type Stirling-like engines (Malone 1931), can be employed in thermoacoustic systems.

The objective of this work is to establish a numerical benchmark for high-fidelity simulations of transcritical thermoacoustic flows, extending previous efforts aimed at the understanding and description of canonical thermoacoustic instabilities (Scalo, Lele & Hesselink 2015; Lin, Scalo & Hesselink 2016; Gupta, Lodato & Scalo 2017). This goal is accomplished by investigating a standing-wave-like thermoacoustically unstable two-dimensional resonator with transcritical CO_2 as the working fluid, building upon Migliorino, Gupta & Scalo (2017), idealizing the set-up used by Alexander *et al.* (2018).

The manuscript is organized as follows: the problem formulation (§ 2) starts with the fluid model and the thermodynamic conditions employed in the Navier–Stokes simulations (§ 2.1), followed by the description of the computational set-up (§ 2.2). The latter includes the full set of governing equations and the numerical set-up employed to solve them (§ 2.2.1), and the thermoviscous wave equations, which guide the geometry optimization (§ 2.2.2). The section ends with a grid sensitivity analysis (§ 2.3), showing the need to include the fully complex eigenvalue in the thermoviscous functions dependence. Real-fluid effects are then discussed in § 3, namely on the frequency and growth rate (§ 3.1), and on the eigenmode shapes in § 3.2, where the reasons for the flattening of the pressure eigenmode amplitude and the smooth transition of the pressure–velocity phase difference at the average location of the pressure node are explained. Then, the energy budgets are discussed in § 4, with a first focus on the acoustic energy budgets (§ 4.1) demonstrating how acoustic power production is increased when approaching the critical point, and then on the total energy budgets (§ 4.2), which show a similar increase also for the heat required. Finally, high amplitude pressure oscillations are first investigated in § 5 by discussing the thermodynamic and convective nonlinearities typical of fluids in transcritical states, and then by describing the limit cycle obtained due to nonlinear minor area losses (§ 6).

Fluid	T_{cr}	p_{cr}	ρ_{cr}	M_m	δ
CO_2	304.1282 K	7.3773 MPa	467.6 kg m^{-3}	44.01 g mol^{-1}	0.225

TABLE 1. Critical properties, molar mass and acentric factor of CO_2.

p_0 (MPa)	7.451	7.746	8.853	10.000	11.066
p_0/p_{cr}	1.01	1.05	1.2	1.356	1.5
Symbol	●	●	●	●	○

TABLE 2. Selected base pressures for the Navier–Stokes simulations.

$\alpha_{cr}M_m^2 p_{cr}/(R_u^2 T_{cr}^2)$	$bp_{cr}/(R_u T_{cr})$	c_1	c_2	β
0.457236	0.0777961	$-1-\sqrt{2}$	$-1+\sqrt{2}$	$0.37464+1.54226\delta-0.26992\delta^2$

TABLE 3. Specific parameters for the PR EoS (2.1).

2. Problem formulation

2.1. *Fluid model*

In this work we have selected carbon dioxide as the working fluid because of its well documented properties (see table 1), making it a good choice for our theoretical investigation. Its transcritical, or PB, state is reached when the fluid is at pressures exceeding its critical value, $p > p_{cr}$, and the temperature varies between $T < T_{cr}$ (pseudo-liquid conditions) and $T > T_{cr}$ (pseudo-gaseous conditions), as figure 2 shows. The density rapidly drops when transitioning from PL to PG conditions (figure 2*a*), hence the spike in the isobaric thermal expansion coefficient (figure 2*b*). However, for increasing pressures, this transition becomes more gradual, and, for large values of the temperature, α_p tends to $1/T$, reverting to a perfect ideal gas behaviour.

The parameter space considered in this study spans the range of base pressures $p_0 = 1.01-1.5p_{cr}$ and temperature differences $\Delta T = T_{hot} - T_{cold}$ up to 200 K (figure 2*a*, see also (2.2), (2.3) and figure 3). For all cases, the value of the cold temperature is $T_{cold} = 293.15$ K. Five base pressures (table 2) are taken into account for the Navier–Stokes simulations.

The equation of state (EoS) of Peng & Robinson (1976) (PR EoS) and the model of Chung *et al.* (1988) for viscosity and thermal conductivity are chosen as the real-fluid model due to their simplicity and ease of implementation. The PR EoS relates pressure, density and temperature as follows:

$$p = \frac{\rho R T}{1-\rho b} - \frac{\rho^2 \alpha_{cr} \alpha}{(1-\rho c_1 b)(1-\rho c_2 b)}, \tag{2.1}$$

where $R = R_u/M_m$, M_m is the molar mass, $R_u = 8.314472$ J mol^{-1} K^{-1} is the universal gas constant, and α is chosen as the one proposed by Soave (1972), $\sqrt{\alpha} = 1+\beta(1-\sqrt{T/T_{cr}})$. The other coefficients are listed in table 3. Notice that the EoS and transport parameter model degrade in accuracy for thermodynamic conditions close to the critical point, while still retaining all the important features of real fluids.

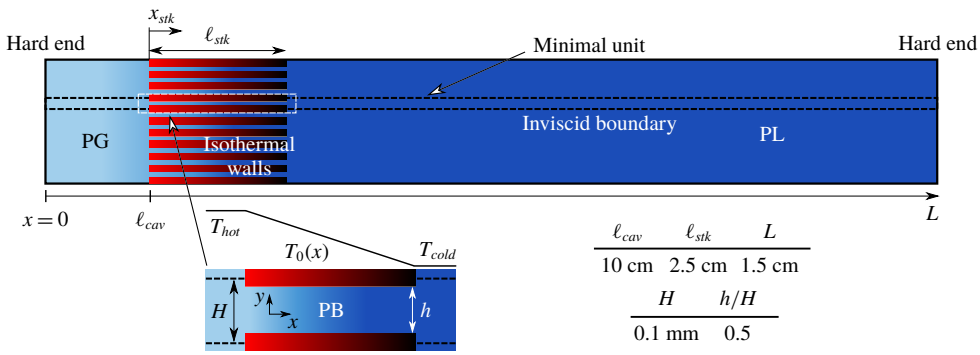

FIGURE 3. Computational set-up (not to scale) with geometrical parameters for minimal unit numerical simulations. Isothermal boundary conditions in the stack are imposed following (2.3). The sidewalls are considered adiabatic.

2.2. *Computational set-up*

The geometrical set-up considered in this study (figure 3) is a two-dimensional resonator composed of a hot cavity, indicated by the subscript *cav*, a thermoacoustic stack, indicated by the subscript *stk*, and a long duct. The whole system is bounded axially by two adiabatic walls at $x=0$ and $x=L$. Fluid in PL conditions (T_{cold}) and PG conditions (T_{hot}), according to the base temperature distribution

$$T_0(x) = \begin{cases} T_{hot} & 0 \leqslant x \leqslant \ell_{cav}, \\ T_{cold} & \ell_{cav} + \ell_{stk} \leqslant x \leqslant L, \end{cases} \tag{2.2}$$

bound the stack ($0 < x_{stk} < \ell_{stk}$), kept at PB conditions by isothermal wall boundary conditions, which impose the following temperature profile:

$$T_0(x) = T_{hot} - \Delta T x_{stk}/\ell_{stk}, \tag{2.3}$$

where $\Delta T = T_{hot} - T_{cold}$. The stack coordinate is defined as

$$x_{stk} = x - \ell_{cav}. \tag{2.4}$$

A canonical minimal unit (Gupta *et al.* 2017) is carved out of this geometry, defining the computational set-up employed for both the linear (frequency domain) and fully nonlinear (Navier–Stokes) numerical analyses. The definition of a minimal unit greatly reduces the computational cost of the Navier–Stokes simulations, which is especially high when employing transcritical fluids, and does not compromise the generality of the results obtained, provided that thermoviscous losses in the parts outside the stack are negligible. Such a condition is true when $\delta_k/R \ll 1$, where R is the hydraulic radius of the resonator and δ_k is the thermal boundary layer thickness (see (5.1)), and is verified for example in Alexander *et al.* (2018), where $\delta_k/R = 3.84 \times 10^{-3}$. This set-up takes into account nonlinear thermodynamic effects and hydrodynamic nonlinear losses due to area jumps, which will be analysed in § 5 and § 6, respectively. Acoustic streaming, transitional turbulence and nonlinear wave steepening are not considered in the Navier–Stokes simulations performed in this study.

2.2.1. *Governing nonlinear equations and numerical set-up*

In this work we consider the fully compressible Navier–Stokes equations, expressed by the conservation laws of mass and momentum,

$$\frac{\partial \rho}{\partial t} + \frac{\partial \rho u_j}{\partial x_j} = 0, \tag{2.5}$$

$$\frac{\partial \rho u_i}{\partial t} + \frac{\partial \rho u_i u_j}{\partial x_j} = -\frac{\partial p}{\partial x_i} + \frac{\partial \tau_{ij}}{\partial x_j}, \tag{2.6}$$

and the evolution equation for pressure (Migliorino & Scalo 2017),

$$\frac{\partial p}{\partial t} + \frac{\partial p u_j}{\partial x_j} = (p - \rho a^2)\frac{\partial u_j}{\partial x_j} + \frac{a^2 \alpha_p}{c_p}\left(\tau_{ij}\frac{\partial u_i}{\partial x_j} - \frac{\partial q_j}{\partial x_j}\right), \tag{2.7}$$

where t is time, x_j and u_j ($j = 1, 2, 3$) are the components of position and velocity, ρ and p are the density and pressure, a is the sound speed, α_p is the isobaric thermal expansion coefficient (1.3) and c_p is the isobaric specific thermal capacity. The Newtonian viscous stress tensor τ_{ij}, according to Stokes's hypothesis, and the Fourier heat flux read, respectively,

$$\tau_{ij} = \mu\left(\frac{\partial u_i}{\partial x_j} + \frac{\partial u_j}{\partial x_i} - \frac{2}{3}\delta_{ij}\frac{\partial u_k}{\partial x_k}\right), \quad q_j = -k\frac{\partial T}{\partial x_j}, \tag{2.8a,b}$$

where δ_{ij} is the Kronecker delta, μ is the dynamic viscosity, k is the thermal conductivity and T is the absolute temperature. Both μ and k depend on density and temperature according to the model of Chung *et al.* (1988).

Equations (2.5), (2.6) and (2.7) are solved with the unstructured spectral difference (SD) solver SD3DVISP, the same as used by Gupta *et al.* (2017) in their thermoacoustics simulations. It has been shown (Migliorino *et al.* 2018) that solving for the total energy equation leads to numerical instability when simulating transcritical flows, due to the loss of mechanical equilibrium at contact discontinuities. Instead, solving the pressure evolution equation (2.7) ensures numerical stability and correct representation of the physics of low Mach number flows (Kawai *et al.* 2015), such as the ones considered in this study. This numerical approach has been tested and validated in Migliorino *et al.* (2018).

The Navier–Stokes numerical simulations are initialized with the following conditions:

$$p = p_0, \quad T = T_0(x), \quad u = \frac{p_0 p_{amp}}{\rho_0 a_0}\sin(\pi x/L), \quad v = 0, \tag{2.9a–d}$$

where $T_0(x)$ is given by (2.2) and (2.3), $\rho_0 = \rho_0(x)$ and $a_0 = a_0(x)$ are the density and sound speed corresponding to p_0 and $T_0(x)$, respectively, and $p_{amp} = 10^{-7}$ for all cases, apart from the ones analysed in § 5 and § 6, for which $p_{amp} = 5 \times 10^{-3}$. Equation (2.9) imposes an initial disturbance in the computational set-up that is thermoacoustically amplified if the system is fluid-dynamically unstable.

The effect of gravity is not taken into account in the present model. In fact, for horizontal or hot-side-up laboratory configuration, gravity will have no significant effect on the oscillating flow dynamics (Alexander *et al.* 2018). If the set-up is placed hot-side-down, boiling might ensue, potentially disrupting any formation of thermoacoustic waves. By placing the hot side up, gravity can also be used to stabilize the mean profiles of temperature and density to avoid any mean flow induced by acoustic nonlinearities.

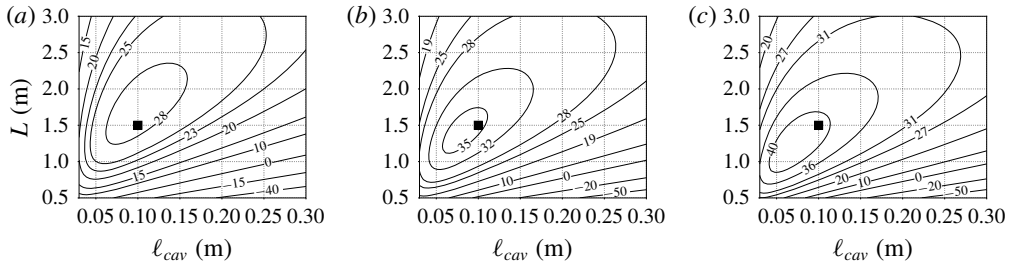

FIGURE 4. Isolevels of thermoacoustic growth rate, α (rad s^{-1}), versus total length, L, and length of the hot cavity, ℓ_{cav} (see figure 3), for $p_0 = 10$ MPa, $\Delta T = 100$ K (*a*), $\Delta T = 125$ K (*b*), and $\Delta T = 150$ K (*c*), with a black square indicating the selected design point. These results are obtained with the solution of the linear system of equations composed by (2.10*a*) and (2.10*b*).

2.2.2. *Linearized thermoviscous wave equations and geometry optimization*

From (2.5), (2.6) and (2.7), it is possible (Rott 1969; Swift *et al.* 1985; Migliorino *et al.* 2017) to obtain, for a generic duct, the frequency-domain equations for the complex volumetric flow rate $\hat{U}$ and pressure $\hat{p}$ (see appendix A),

$$\sigma \hat{U} = -\frac{A}{\rho_0 F_\nu}\frac{\mathrm{d}\hat{p}}{\mathrm{d}x}, \tag{2.10a}$$

$$\sigma \hat{p} = \frac{\rho_0 a_0^2}{A F_k}\left(\Theta \Phi_{\mathcal{P}} - \frac{\mathrm{d}}{\mathrm{d}x}\right)\hat{U}, \tag{2.10b}$$

where $\sigma = \alpha + \mathrm{i}\omega$ is the complex eigenvalue with growth rate α and angular frequency ω, and

$$\Phi_{\mathcal{P}} = \frac{1}{1 - Pr_0}\frac{f_k - f_\nu}{1 - f_\nu}, \quad F_\nu = \frac{1}{1 - f_\nu}, \quad F_k = 1 + (\gamma_0 - 1) f_k, \tag{2.11a–c}$$

where the thermoviscous functions f_ν and f_k depend on σ, the duct geometry, Prandtl number and kinematic viscosity (see (A 21) and (A 31)). Base state quantities are a function of the axial coordinate x only and are denoted with a subscript 0; $\nu_0 = \mu_0/\rho_0$ is the kinematic viscosity, $\gamma_0 = c_{p0}/c_{v0}$ is the ratio of specific heats and $Pr_0 = c_{p0}\mu_0/k_0$ is the Prandtl number. Furthermore, A is in general the cross-sectional area of the duct, intended per unit depth for the geometry employed in this study. When the linearized equations are solved, the flow field is considered at uniform base pressure p_0.

Equations (2.10*a*) and (2.10*b*) are discretized on a staggered uniform grid with second-order numerical operators (Lin *et al.* 2016; Gupta *et al.* 2017) and solved with a shift-Arnoldi algorithm. For all the results in this paper, we will always refer to the first resonant mode of the system.

The minimal unit computational set-up is optimized, based on the linear theory, for three values of ΔT (figure 4), resulting in the geometrical parameters listed in figure 3. The optimization is performed here visually on the plots of the growth rates and provides a geometry for which thermoacoustic instability appears for only approximately $\Delta T = 25$ K. Other values of p_0 or ΔT considered in the optimization would lead to different geometries, which are not considered in this study.

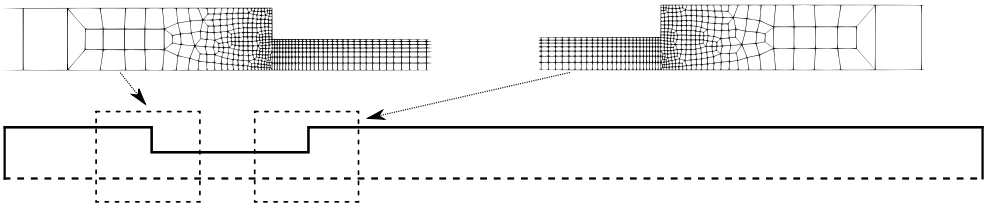

FIGURE 5. Illustrations of portions of the unstructured mesh for grid B (see table 4), close to area changes, used for the Navier–Stokes simulations. This mesh has total number of elements $N_{el} = 2635$.

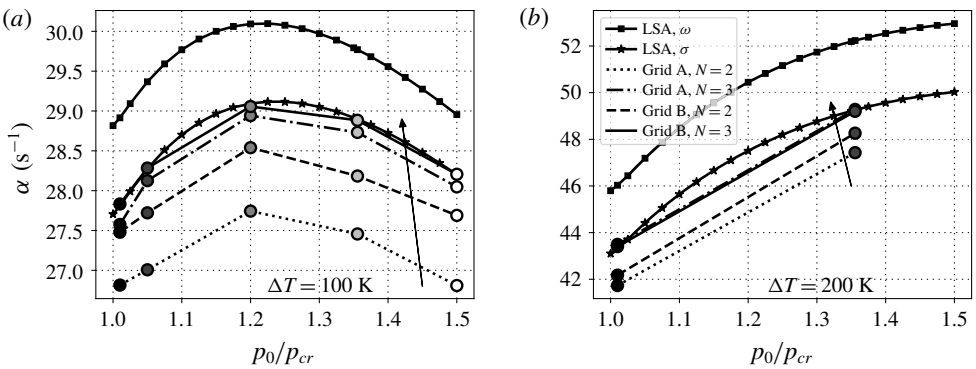

FIGURE 6. Growth rate versus reduced base pressure for $\Delta T = 100$ K (*a*) and $\Delta T = 200$ K (*b*), for the different grid resolutions in table 4. Circles connected by lines are obtained from the Navier–Stokes simulations, with arrows indicating increasing resolution (see legend in (*b*)). Results labelled with 'LSA, ω' and 'LSA, σ' are obtained from linear stability analysis (LSA) with thermoviscous functions only dependent on ω (2.13), and on $\alpha + \mathrm{i}\omega$ (2.12), respectively.

	Grid A ($N_{el} = 1135$)	Grid B ($N_{el} = 2635$)
	N_{dof}	N_{dof}
$N = 2$	4540	10 540
$N = 3$	10 215	23 715

TABLE 4. Number of degrees of freedom, $N_{dof} = N^2 N_{el}$, for the two grids considered in this study, and for two numbers of solution points N inside each element.

2.3. *Grid sensitivity analysis*

The Navier–Stokes simulations are carried out on an unstructured mesh discretizing only half of the minimal unit (figure 5), exploiting the symmetry of the flow field with respect to the centre line of the domain. Two different grids are considered (table 4): A (coarse) and B (fine). The order of accuracy of the polynomial reconstruction is fixed with N, indicating the number of points inside each element. For each grid, $N = 2$ and $N = 3$ are chosen.

A grid sensitivity study on the linear growth rate indicates converging behaviour (figure 6) of the data from the Navier–Stokes simulations, from grid A with $N = 2$ to

the finest resolution employed (grid B and $N=3$), towards the growth rates predicted by the linear theory. However, an important remark is that to achieve such agreement the thermoviscous functions in (A 21) and (A 31) have to depend on the full eigenvalue σ, and not only on its imaginary part ω, otherwise linear theory overpredicts the growth rate. In fact, the normalization for the transverse spatial coordinate r, equation (A 16), which reads

$$\eta=\sqrt{\frac{\sigma}{\nu_0}}r=\sqrt{2\mathrm{i}+2\frac{\alpha}{\omega}}\frac{r}{\delta_\nu}, \tag{2.12}$$

where δ_ν is defined in (5.1), includes both the growth rate, α, and angular frequency, ω, information. Previous studies restricted to ideal gas (Rott 1969; Swift *et al.* 1985; Lin *et al.* 2016; Gupta *et al.* 2017) have made the assumption that $\alpha\ll\omega$, i.e. $\sigma\approx\mathrm{i}\omega$, which cannot be used here (see appendix B), yielding

$$\eta=\sqrt{\frac{\mathrm{i}\omega}{\nu_0}}r=\sqrt{2i}\frac{r}{\delta_\nu}=(i+1)\frac{r}{\delta_\nu}. \tag{2.13}$$

Adopting $N=3$ solution points yields approximately the same growth rates for grids A and B (especially for $\Delta T=200$ K, for which the two results are almost identical). Furthermore, an almost equal number of total degrees of freedom N_{dof} entails different results depending on the order of the polynomial reconstruction inside each element: grid A with $N=3$ ($N_{dof}=10\,215$) provides a better estimate of the growth rates compared to grid B with $N=2$ ($N_{dof}=10\,540$). This justifies the use of high-order numerics in the simulation of thermoacoustic instabilities.

Frequencies were found to be not very sensitive to grid resolution, as they are determined primarily from inviscid processes.

3. Real-fluid effects on frequency, growth and eigenmodes

3.1. *Real-fluid effects on frequency and growth rate*

The frequency of the thermoacoustic response is dependent on the ΔT across the stack for all base pressures p_0 considered (figure 7). The largest values of ω are obtained for values of ΔT below 5 K, for which most of the system is filled with pseudo-liquid, which has a high speed of sound. Then, for increasing ΔT, the frequency drops by approximately 40 %, with sharper variations at near-critical conditions, due to the drop in sound speed characteristic of PB fluids. For higher values of ΔT, the frequency increases approximately in a linear fashion, due to the appearance of fluid in near-ideal gas state, for which the speed of sound increases with temperature, in the hot cavity. Keeping the same ΔT across the stack, for increasing base pressures, the frequency increases approximately with a linear trend, entailing changes of 15 % from $p/p_{cr}=1.01$ to 1.5. Thermoacoustic oscillations featuring ideal gases show much milder dependence of the frequency on the thermodynamic conditions (Lin *et al.* 2016; Gupta *et al.* 2017). The grid requirements necessary to capture the correct frequency are less stringent than the ones needed for numerical convergence of the growth rates (figure 6).

The thermoacoustic growth rate strongly depends on the ΔT across the stack (figure 8), because large values of ΔT increase the thermoacoustic gain Θ, which in turn controls the acoustic energy production (discussed more in detail in § 4.1). For all base pressures considered, the minimum ΔT required for the onset of instability

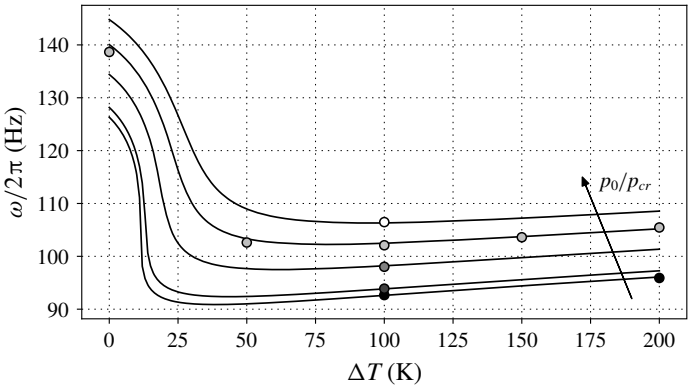

FIGURE 7. Frequency versus ΔT for the five base pressures in table 2. Solid lines indicate results from linear theory, symbols are data extracted from the Navier–Stokes simulations (with grid B and resolution $N = 2$, see table 4).

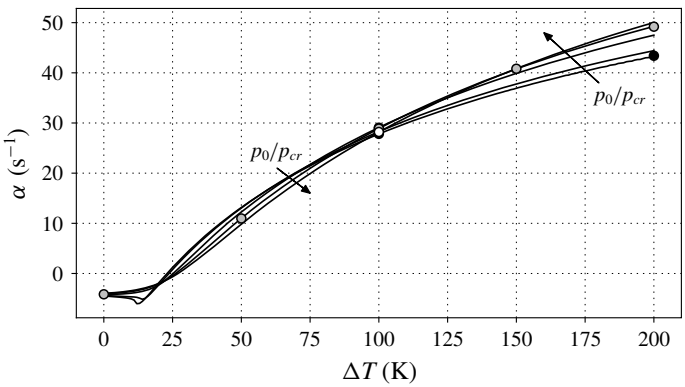

FIGURE 8. Growth rate versus ΔT for the five base pressures in table 2. Solid lines indicate results from linear theory, symbols are data extracted from the Navier–Stokes simulations (with grid B and resolution $N = 3$, see table 4).

(positive growth rate) is only approximately 25 K, much less than what is usually needed in standard thermoacoustic systems employing perfect ideal gases (Swift 1992; Lin *et al.* 2016; Gupta *et al.* 2017). The configuration with base pressure closer to the critical pressure requires the lowest ΔT (=23 K) to be thermoacoustically unstable.

A non-monotonic variation in the growth rate is present right before $\Delta T = 15$ K, for $p_0 = 1.01p_{cr}$ and $p_0 = 1.05p_{cr}$, due to the occurrence of PB conditions inside the stack, whereas higher values of p_0 entail the monotonic trends expected in ideal gases. From the onset of instability onwards, increasing ΔT always corresponds to a rise in growth rate, with the highest values obtained in near-critical conditions (for the lowest values of p_0 considered) until approximately 100 K; after such a value, the growth rate monotonically increases with pressure. The latter is a surprising result if one simply relies on the intuition that higher base density gradients, achieved at lower pressures, are expected to boost thermoacoustic energy production (Migliorino *et al.* 2017). Instead, for example, at $\Delta T = 100$ K the growth rate varies in a non-monotonic manner with different base pressures, showing a maximum around $p_0 = 1.25p_{cr}$ (figure 6*a*), which will be explained in § 4.1. These effects are not

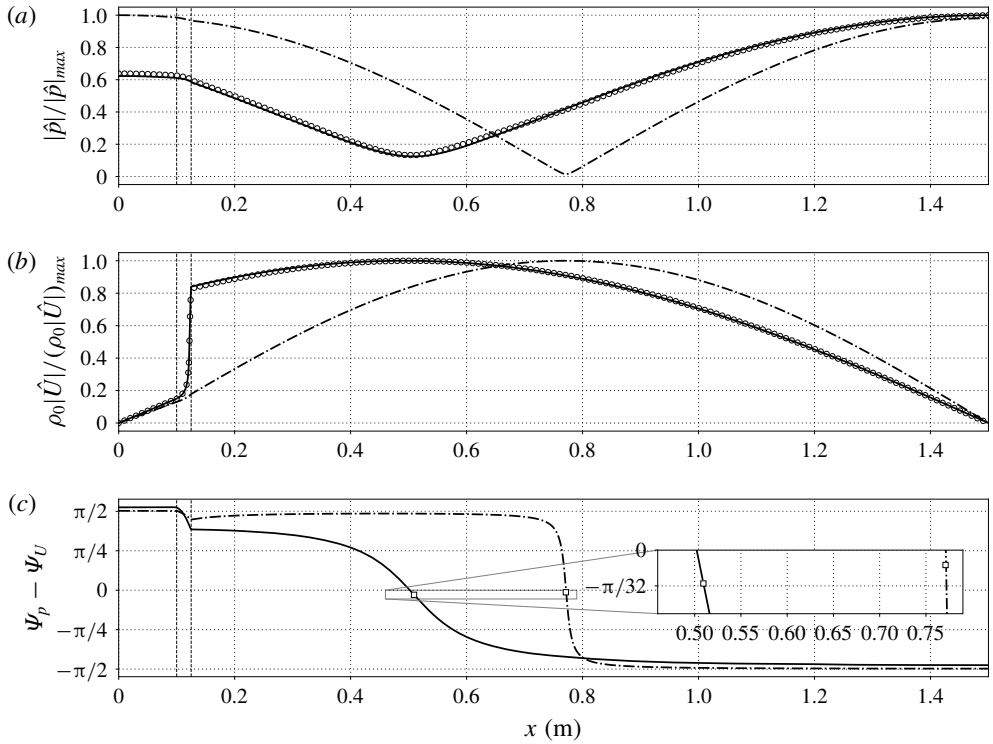

FIGURE 9. Axial distribution of pressure (*a*) and mass flow rate (*b*) dimensionless amplitudes and phasing between $\hat{p}$ and $\hat{U}$ (*c*), for $\Delta T = 200$ K and $p_0 = 10$ MPa: linear theory (solid lines), data extracted from the Navier–Stokes simulations (circles). Dashed-dotted lines indicate eigenmodes obtained from linear theory with the assumption of thermally perfect ideal gas. Vertical dashed lines indicate locations of abrupt area change (see figure 3). The squares in (*c*) indicate values of phase difference at the location of minimum pressure amplitude.

usually present in thermoacoustic systems employing ideal gases (Swift 1992; Lin *et al.* 2016; Gupta *et al.* 2017).

Overall, the frequencies and growth rates extracted from the Navier–Stokes simulations confirm the predictions obtained from the linear theory, hence validating the linear ansatz despite the large gradients in the base state and the extreme thermodynamic conditions.

3.2. *Real-fluid effects on eigenmodes*

Strong real-fluid effects, due to the sharp base density gradients present in the stack, entail a deviation of the eigenmodes shapes from the classic ideal gas axial profiles (figure 9*a*,*b*). For $\Delta T = 200$ K, the overall spatial distribution of the eigenmodes, and their matching with Navier–Stokes data, were found not to be significantly dependent on p_0.

The spatial variation of the amplitude of the pressure eigenmode in the linear regime (figure 9*a*) is much more gradual than its ideal gas counterpart. This can be explained

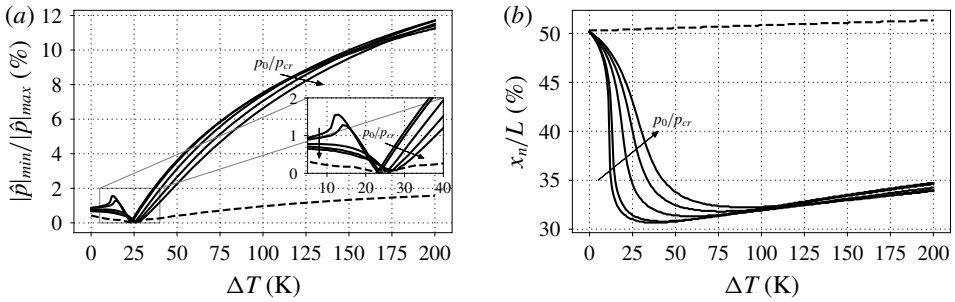

FIGURE 10. Data from linear stability theory on pressure eigenmode amplitude: relative magnitude (*a*) and location (*b*) of its minimum. Solid lines are for real-fluid EoS (for all base pressures in table 2), and the dashed line indicates thermally perfect ideal gas EoS (for $p_0 = 10$ MPa only).

(appendix B) as a result of the closure of the acoustic energy budgets, yielding

$$\frac{|\hat{p}|_{min}}{|\hat{p}|_{max}} \propto \frac{|\alpha|}{\omega}, \tag{3.1}$$

regardless of the EoS. A large growth-rate-to-frequency ratio is, however, typical of transcritical thermoacoustic oscillations (see figure 21*b*), with $|\hat{p}|_{min}/|\hat{p}|_{max}$ values up to 12 % (figure 10*a*). The same configuration, with the assumption of a thermally perfect ideal gas, is characterized by $|\hat{p}|_{min}/|\hat{p}|_{max}$ values of at most 2 %.

Furthermore, during the linear growth regime, a stationary node does not exist (see appendix B for more details), since the pressure eigenmode is zero at different axial locations in time. The average location of the pressure node is referred to as $x = x_{|p|_{min}} = x_n$. In the transcritical case, the pressure eigenmode amplitude presents its minimum always shifted towards the stack (showing a minimum of approximately 31 % of the total length, see figure 10*b*), contrary to the ideal gas case, for which x_n can reach a maximum of $0.51L$. The trend of x_n versus ΔT resembles the one of frequency versus ΔT (figure 7). This is due to a local decrease in wavelength connected to the lower speed of sound of PB and PG conditions compared to PL conditions.

In addition, the most intense mass transport events are expected inside the stack, where the axial gradient of $\rho_0|U|$ is maximum, which is where transcritical conditions are achieved (figure 9*b*). Such events, if pressure amplitudes are sufficiently high, entail convective nonlinearities (analysed in § 5).

Another quantity of interest is the phasing between $\hat{p}$ and $\hat{U}$: $\Psi_p - \Psi_U$ (figure 9*c*). The axial profile of $\Psi_p - \Psi_U$, for the ideal gas configuration, is consistent with similar trends reported by Yazaki *et al.* (1998), who observed a sharp change from $\pi/2$ to approximately $-\pi/2$. Instead, for the transcritical case, $\Psi_p - \Psi_U$ shows a much milder transition inside the resonator. Moreover, the value of $\Psi_p - \Psi_U$ at $x = x_n$ (see inset in figure 9*c*) is never exactly zero in the presence of thermoacoustic growth, and is in magnitude higher for the transcritical fluid than for the ideal gas case. In fact, it can be shown that (appendix B)

$$\Psi_{p_n} - \Psi_{U_n} = -\arctan\left(\frac{\alpha}{\omega}\right), \tag{3.2}$$

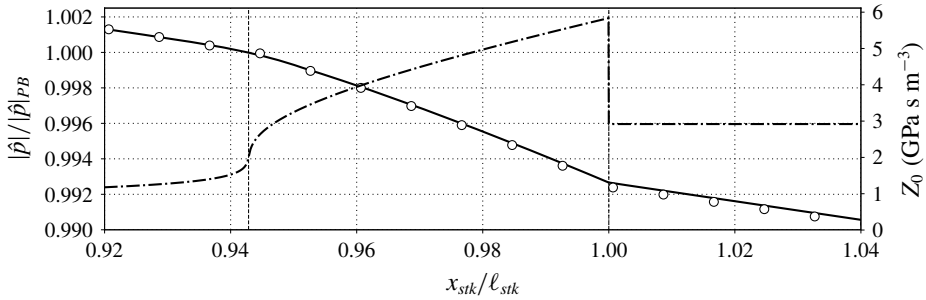

FIGURE 11. Axial distribution of dimensionless pressure amplitudes (left y axis), and base acoustic impedance (right y axis), for $\Delta T = 200$ K and $p_0 = 1.01p_{cr}$: linear theory (solid line), data extracted from the Navier–Stokes simulations (circles), and base acoustic impedance (dashed dotted line). The vertical dashed line on the left indicates PB conditions, achieved at $x_{stk}/\ell_{stk} = 0.942$, while the one on the right denotes the end of the stack ($x_{stk}/\ell_{stk} = 1$).

indicating that the pressure–velocity phase difference is significantly different than zero at $x = x_n$ for transcritical flows, due to the high value of α/ω. This means that, at $x = x_n$, pressure and flow rate are generally more out of phase for transcritical fluids than for ideal gases. However, due to the smooth spatial variation in phasing, transcritical fluids exhibit a wider interval, centred around x_n, where travelling-wave-like phasing is present.

We finally concentrate our attention towards the end of the stack, where we observe two changes in derivative of the pressure eigenmode amplitude (figure 11). These can be explained by considering the axial profiles of the acoustic impedance Z_0, obtained as the ratio of the specific acoustic impedance and the duct area,

$$Z_0 = \frac{\rho_0 a_0}{A}. \tag{3.3}$$

At $x_{stk}/\ell_{stk} = 1$, since no discontinuity in base state quantities is present (uniform $\rho_0 a_0$), the area change is responsible for a jump in Z_0, resulting in a local change in $\mathrm{d}|\hat{p}|/\mathrm{d}x$, also for the ideal gas case (not shown). However, no variations in area are present inside the stack, but in the vicinity of the pseudo-boiling region great variations of base density and speed of sound produce a pseudo-jump in Z_0, which entails a gradual change in the spatial derivative of the pressure eigenmode amplitude (and of the mass flow rate, not shown). This rapid change in Z_0 at transcritical conditions effectively acts on the eigenmodes like a continuous change in geometry, which is a peculiar real-fluid effect not present for higher base pressures or ideal gases, characterized by milder variations of thermodynamic properties.

The large difference in acoustic impedance between fluid in PL conditions and fluid in the hot cavity is also responsible for the presence of the maximum of pressure on the right end side of the domain for the real gas configuration (figure 9*a*). For ideal gases, instead, the acoustic impedance in the hot cavity can be higher than the one evaluated on the right of the stack, causing the maximum pressure amplitude to be at $x = 0$.

4. Energy budgets in the linear regime

The mechanisms of conversion from heat to acoustic energy occur inside the stack, where a Lagrangian fluid parcel experiences a thermodynamic cycle, driven

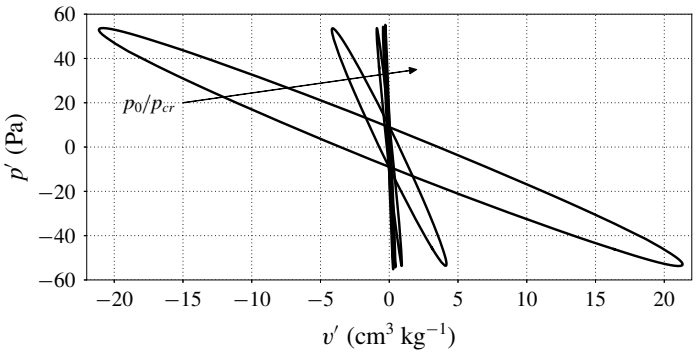

FIGURE 12. Fluctuating pressure plotted against specific volume fluctuation of a Lagrangian fluid parcel, for all base pressures of table 2 and $\Delta T = 100$ K, extracted with the aid of the linear theory. Initial position of the Lagrangian parcel is at the centre line of the stack and at PB conditions ($x = 12.21$, 12.17, 12.019, 11.88, 11.77 cm for increasing values of p_0). All cycles are taken at the same pressure amplitude and are traversed clockwise.

by the harmonic pressure oscillations, with expansions and contractions accompanied by heating and cooling. The resulting Lagrangian pressure–volume cycle, traversed clockwise, indicates mechanical power production (figure 12), which is strongly dependent on the spatial variation in the fluid's base state resulting from the imposed mean temperature distribution (2.2). As base pressures approach the critical pressure, transcritical conditions entail sharper spatial gradients in base density, which in turn cause larger volume fluctuations for the same pressure oscillation amplitude, hence generating more power due to the larger area encompassed by the Lagrangian pressure–volume cycle.

4.1. *Acoustic energy budgets*

Multiplying (2.10*a*) by $\hat{U}^*$ and (2.10*b*) by $\hat{p}^*$, where a superscript $*$ indicates the complex conjugate, yields, after rearranging,

$$\sigma \overline{\kappa} F_v A = -\frac{1}{2}\frac{\mathrm{d}\hat{p}}{\mathrm{d}x}\hat{U}^*, \tag{4.1a}$$

$$\sigma \overline{\varepsilon} F_k A = \frac{\Theta \Phi_{\mathcal{P}}}{2}\hat{U}\hat{p}^* - \frac{1}{2}\hat{p}^*\frac{\mathrm{d}\hat{U}}{\mathrm{d}x}, \tag{4.1b}$$

which are the equations for the acoustic kinetic energy density and acoustic potential energy density, defined by

$$\overline{\kappa} = \frac{\rho_0}{2}\frac{|\hat{U}|^2}{A^2}, \quad \overline{\varepsilon} = \frac{1}{2}\frac{|\hat{p}|^2}{\rho_0 a_0^2}, \tag{4.2a,b}$$

respectively, both with units of energy per unit volume. Taking the real part of the addition of (4.1*a*) with (4.1*b*), and using the properties $\mathrm{Re}\{\phi\psi\} = \mathrm{Re}\{\phi\}\mathrm{Re}\{\psi\} - \mathrm{Im}\{\phi\}\mathrm{Im}\{\psi\}$, and $\mathrm{Re}\{\phi - \phi^*\} = 0$, where ϕ, ψ are two generic complex numbers, yields

$$\alpha\overline{\mathcal{E}} + \frac{\mathrm{d}\overline{\dot{W}}}{\mathrm{d}x} = \overline{\mathcal{P}} - \overline{\mathcal{D}}, \tag{4.3}$$

where the acoustic energy density is defined as

$$\overline{\mathcal{E}} = A(\mathrm{Re}\{F_\nu\}\overline{\kappa} + \mathrm{Re}\{F_k\}\overline{\varepsilon}), \tag{4.4}$$

which has dimensions of an energy per unit length, the acoustic power is

$$\overline{\dot{W}} = \tfrac{1}{2}\mathrm{Re}\{\hat{p}\,\hat{U}^*\}, \tag{4.5}$$

which has dimensions of an energy per unit time, the production of acoustic energy density is

$$\overline{\mathcal{P}} = \frac{\Theta}{2}[\mathrm{Re}\{\Phi_{\mathcal{P}}\}\mathrm{Re}\{\hat{p}^*\hat{U}\} - \mathrm{Im}\{\Phi_{\mathcal{P}}\}\mathrm{Im}\{\hat{p}^*\hat{U}\}], \tag{4.6}$$

and its dissipation is

$$\overline{\mathcal{D}} = -\omega A(\mathrm{Im}\{F_\nu\}\overline{\kappa} + \mathrm{Im}\{F_k\}\overline{\varepsilon}), \tag{4.7}$$

both with dimensions of power per unit length. The weights of $\mathrm{Re}\{\hat{p}^*\hat{U}\}$ and $\mathrm{Im}\{\hat{p}^*\hat{U}\}$ in (4.6), $\mathrm{Re}\{\Phi_{\mathcal{P}}\}$ and $-\mathrm{Im}\{\Phi_{\mathcal{P}}\}$, respectively, are strongly dependent on Pr_0, but never negative (Migliorino *et al.* 2017).

Integrating (4.3) axially along the domain yields

$$\alpha = \mathcal{R}/\Sigma, \tag{4.8}$$

where the Rayleigh index (Gupta *et al.* 2017) is

$$\mathcal{R} = \int_0^L (\overline{\mathcal{P}} - \overline{\mathcal{D}})\,\mathrm{d}x, \tag{4.9}$$

and the total acoustic energy is

$$\Sigma = \int_0^L \overline{\mathcal{E}}\,\mathrm{d}x, \tag{4.10}$$

and where hard-wall boundary conditions have been taken into account (the acoustic power is zero at $x = 0$ and $x = L$). Once the eigenvalue problem in (2.10) is solved, it is possible to directly evaluate all the variables in (4.5), (4.6) and (4.7), allowing us to compute the growth rate from (4.8). This procedure has been carried out for all the configurations considered in this work and the growth rate hence obtained is in excellent agreement with the one computed from the numerical eigenvalue solution of (2.10). Indeed, the pointwise acoustic energy budgets in (4.3) are closed (figure 13*e*), corroborating the validity of the data extracted from the linear theory.

As the base pressure increases, transcritical conditions are achieved for a higher temperature (see figure 2*b*), shifting the location of fluid in PB conditions towards the hot side of the stack, and yielding a lower maximum of $|\Theta|$ (figure 13*b*). This directly affects the location and intensity of the spike of the acoustic energy production (figure 13*c*, equation (4.6)). The boost of production obtained for values of p_0 approaching p_{cr} is, however, also accompanied by a similar increase in acoustic dissipation (figure 13*c*), due to the high values of Prandtl number typical of transcritical conditions (figure 13*a*). The nonlinear trends exhibited by production and dissipation of acoustic energy throughout the stack are responsible for the

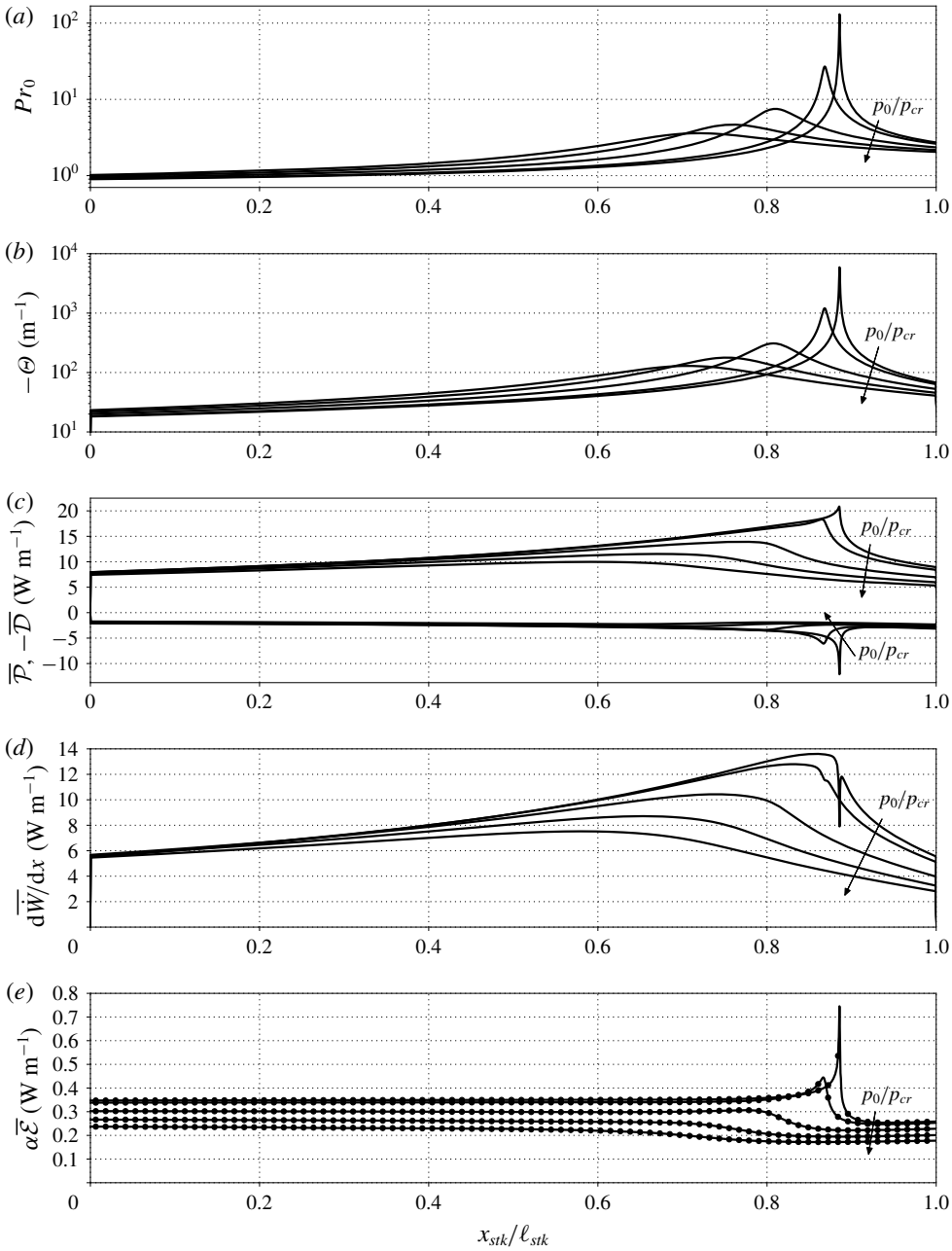

FIGURE 13. Base state quantities and acoustic energy budgets terms inside the stack ($x_{stk} = [0,\ \ell_{stk}]$) from linear theory, for $\Delta T = 100$ K and the base pressures in table 2: (*a*) base Prandtl number; (*b*) minus thermoacoustic gain (1.1); (*c*) acoustic energy production ((4.6), positive values) and minus acoustic energy dissipation ((4.7), negative values); (*d*) axial gradient of acoustic power (4.5); (*e*) $\overline{\mathcal{P}} - \overline{\mathcal{D}} - \overline{\mathrm{d}\dot{W}/\mathrm{d}x}$ (filled circles) and $\alpha\overline{\mathcal{E}}$ (solid lines, equation (4.4)), see (4.3). All quantities correspond to maximum pressure oscillation amplitude of 100 kPa, fixed for all base pressures.

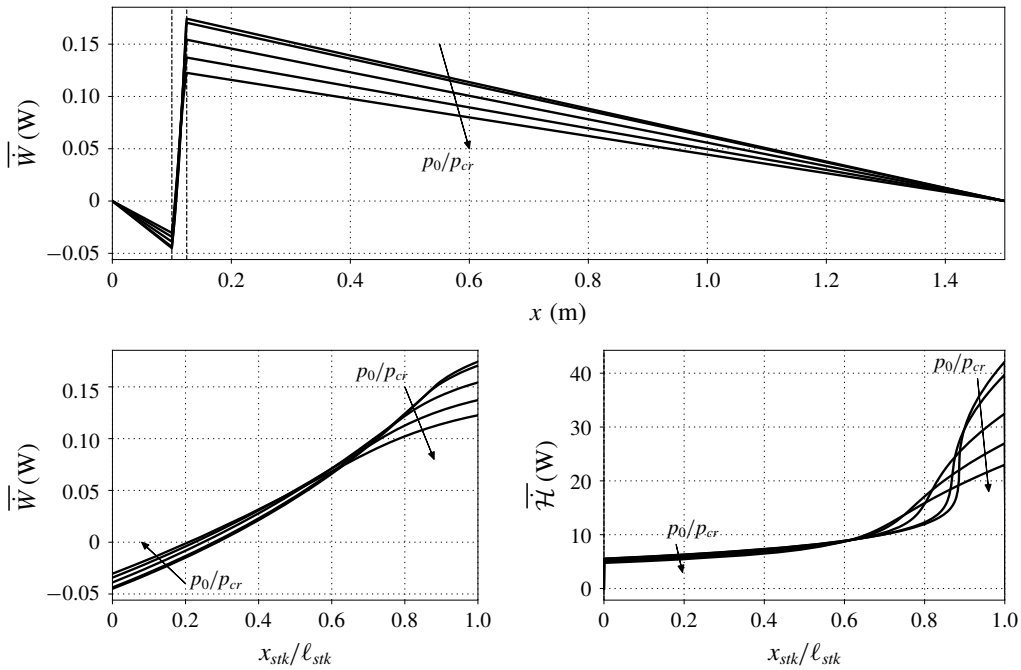

FIGURE 14. (*a*) Acoustic power (4.5) in the whole domain; (*b*) acoustic power in the stack; (*c*) total energy flux (4.19) in the stack. Data are taken from the linear stability theory, for $\Delta T = 100$ K and all base pressures of table 2. The values on the y axis correspond to a maximum pressure oscillation amplitude of 100 kPa, fixed for all base pressures.

non-monotonic behaviour observed for the growth rate as a function of p_0/p_{cr} in figure 6(*a*). Furthermore, the derivative of the acoustic power presents a maximum at PB conditions for higher base pressures, and a local minimum for $p_0 = 1.01p_{cr}$ and $p_0 = 1.05p_{cr}$. The acoustic energy density is mostly uniform in the stack, apart from the PB region where it presents a spike (figure 13*e*), gradually reduced by increasing the base pressures away from the critical point.

For all values of p_0, the acoustic power flows away from the stack, reaching boundary values of zero due the imposed hard wall boundary conditions at both ends of the device (figure 14*a*), while inside the stack (figure 14*b*) a positive gradient (see figure 13*d*) confirms acoustic power production. The trends of the acoustic power inside the stack confirm the intuitive conclusion, drawn from figure 12, that near-critical base pressures entail higher power production in the linear regime. However, the heat input required for sustaining the same pressure oscillations at values of p_0 closer to p_{cr} is expected to be higher, given the spike in thermal capacities typical of transcritical conditions.

4.2. *Total energy budgets*

The evolution equation for total energy in two dimensions reads

$$\frac{\partial \rho E}{\partial t} + \frac{\partial \rho H u}{\partial x} + \frac{\partial \rho H v}{\partial y} = \frac{\partial u_i \tau_{i1}}{\partial x} + \frac{\partial u_i \tau_{i2}}{\partial y} - \frac{\partial q_1}{\partial x} - \frac{\partial q_2}{\partial y}, \tag{4.11}$$

where $E = e + (u^2 + v^2)/2$ is the specific total energy, sum of specific internal energy and specific kinetic energy, $H = E + p/\rho$ is the specific total enthalpy, and the other quantities are the same as in (2.7). Integrating (4.11) across the stack pore area, for a two-dimensional rectilinear geometry, yields

$$\frac{\partial}{\partial t}\int_{-h/2}^{h/2} \rho E \,\mathrm{d}y + \frac{\partial}{\partial x}\int_{-h/2}^{h/2} \rho H u \,\mathrm{d}y = \int_{-h/2}^{h/2} \frac{\partial u_i \tau_{i1}}{\partial x}\,\mathrm{d}y - \frac{\partial}{\partial x}\int_{-h/2}^{h/2} q_1 \,\mathrm{d}y - [q_2]_{-h/2}^{h/2}, \quad (4.12)$$

where we accounted for $u = v = 0$ at $y = \pm h/2$. Introducing the cycle averaging operator

$$\overline{(\cdot)} = \frac{\omega}{2\pi}\int_0^{2\pi/\omega} (\cdot)\,\mathrm{d}t, \quad (4.13)$$

where time 0 indicates the arbitrary beginning of an acoustic cycle, equation (4.12) becomes

$$\int_{-h/2}^{h/2} \frac{[\rho E]_0^{2\pi/\omega}}{2\pi/\omega}\,\mathrm{d}y + \frac{\partial}{\partial x}\int_{-h/2}^{h/2} (\overline{\rho H u} + \overline{q_1})\,\mathrm{d}y = \int_{-h/2}^{h/2} \overline{\frac{\partial u_i \tau_{i1}}{\partial x}}\,\mathrm{d}y - [\overline{q_2}]_{-h/2}^{h/2}. \quad (4.14)$$

Scaling arguments provided by Swift (1988) allow us to neglect the energy change due to viscous dissipation, first term on the right-hand side of (4.14), which, neglecting terms of third order, becomes

$$-[\overline{q_2}]_{-h/2}^{h/2} = \int_{-h/2}^{h/2} \frac{[\rho E]_0^{2\pi/\omega}}{2\pi/\omega}\,\mathrm{d}y + \frac{\partial \overline{\dot{\mathcal{H}}}}{\partial x}, \quad (4.15)$$

where

$$\overline{\dot{\mathcal{H}}} = \int_{-h/2}^{h/2} \left(\overline{\rho h u}\,\mathrm{d}y - \overline{k\frac{\partial T}{\partial x}}\right)\mathrm{d}y \quad (4.16)$$

is the fluid's time-averaged total energy flux. Integrating (4.15) axially along the stack, with 1 indicating the axial coordinate of its beginning and 2 its end (see figure 15), yields

$$\overline{\dot{Q}} = \int_{x_1}^{x_2}\int_{-h/2}^{h/2} \frac{[\rho E]_0^{2\pi/\omega}}{2\pi/\omega}\,\mathrm{d}y\,\mathrm{d}x + \overline{\dot{\mathcal{H}}}_2 - \overline{\dot{\mathcal{H}}}_1, \quad (4.17)$$

where the time-averaged heat exchange through the walls is

$$\overline{\dot{Q}} = -\int_{x_1}^{x_2} [\overline{q_2}]_{-h/2}^{h/2}\,\mathrm{d}x = 2\int_{x_1}^{x_2} \overline{\left(k\frac{\partial T}{\partial y}\right)}_{h/2}\,\mathrm{d}x, \quad (4.18)$$

where we assumed a symmetric temperature profile around $y = 0$. Equation (4.17) shows that the boundary heat flux is absorbed by the fluid in the form of time-averaged total energy flux difference between the two stack extremities.

The frequency domain expression for the time-averaged energy flux (4.16) is (Swift 1988; Ward, Clark & Swift 2012),

$$\overline{\dot{\mathcal{H}}} = \frac{1}{2}\mathrm{Re}\left\{\hat{p}\hat{U}^*\left(1 - \frac{\alpha_{p_0} T_0 (f_k - f_\nu^*)}{(1 + Pr_0)(1 - f_\nu^*)}\right)\right\} + \frac{\rho_0 a_0^2 \Theta |\hat{U}|^2}{2AG_0\omega|1 - f_\nu|^2}\mathrm{Im}\left\{\frac{f_\nu^* Pr_0 + f_k}{1 - Pr_0^2}\right\} + H_k, \quad (4.19)$$

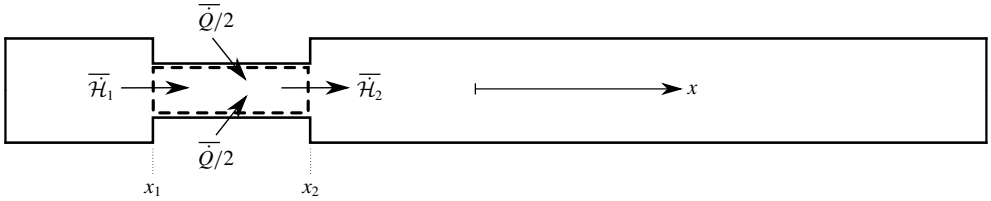

FIGURE 15. Control volume (thick dashed lines) used for the total energy balance inside the stack pore in the minimal unit set-up described by figure 3.

where

$$H_k = -Ak_0 \frac{\mathrm{d}T_0}{\mathrm{d}x} \tag{4.20}$$

is the conductive axial heat flux, and where

$$G = \frac{\alpha_p a^2}{c_p} = \frac{\gamma - 1}{\alpha_p T}, \tag{4.21}$$

is the Grüneisen parameter, which reverts to $\gamma - 1$ for ideal gases, and which is described by Swift *et al.* (1985) as the ratio between the work parameter $\gamma - 1$ and the heat parameter $\alpha_p T$. For our configuration, $\overline{\dot{\mathcal{H}}}$ is equal to the acoustic power when computed outside of the stack.

The profile of $\overline{\dot{\mathcal{H}}}$ inside the stack (figure 14*c*) shows the cumulative time-averaged heat in Watts required from the solid walls of the stack to sustain the fluid oscillations (ignoring the first term on the right-hand side of (4.17)). The axial derivative of $\overline{\dot{\mathcal{H}}}$ represents the pointwise heat per unit length (W m^{-1}) injected into the fluid. The highest wall heat flux is required to sustain carbon dioxide oscillating around its PB state, followed by fluid in PL and PG conditions, on its right and left, respectively, which is a hierarchy consistent with the one of the isobaric specific heat capacities of each thermodynamic condition. For a given ΔT, conditions closer to the critical point do produce more acoustic power, but also require more energy to be sustained.

The efficiency of the thermal-to-acoustic energy transformation can be computed by dividing the produced acoustic power to the total energy required by the stack,

$$\eta = \frac{\overline{\dot{W}}_2 - \overline{\dot{W}}_1}{\overline{\dot{Q}}}. \tag{4.22}$$

This estimate can be more accurately performed if a limit cycle is present (to cancel the unsteady term in (4.17)). In order to do so, nonlinear effects need to be considered, as done in the remainder of the manuscript.

5. Thermodynamic nonlinearities at moderate pressure amplitudes

For moderate pressure amplitude values (of approximately 1 % p_0), rapid, asymmetric and strong density oscillations are observed for $p_0/p_{cr} = 1.01$ (figure 16*a*), close to the right-hand side of the stack, where PB conditions allow large variations of thermodynamic properties from small temperature perturbations. At the beginning

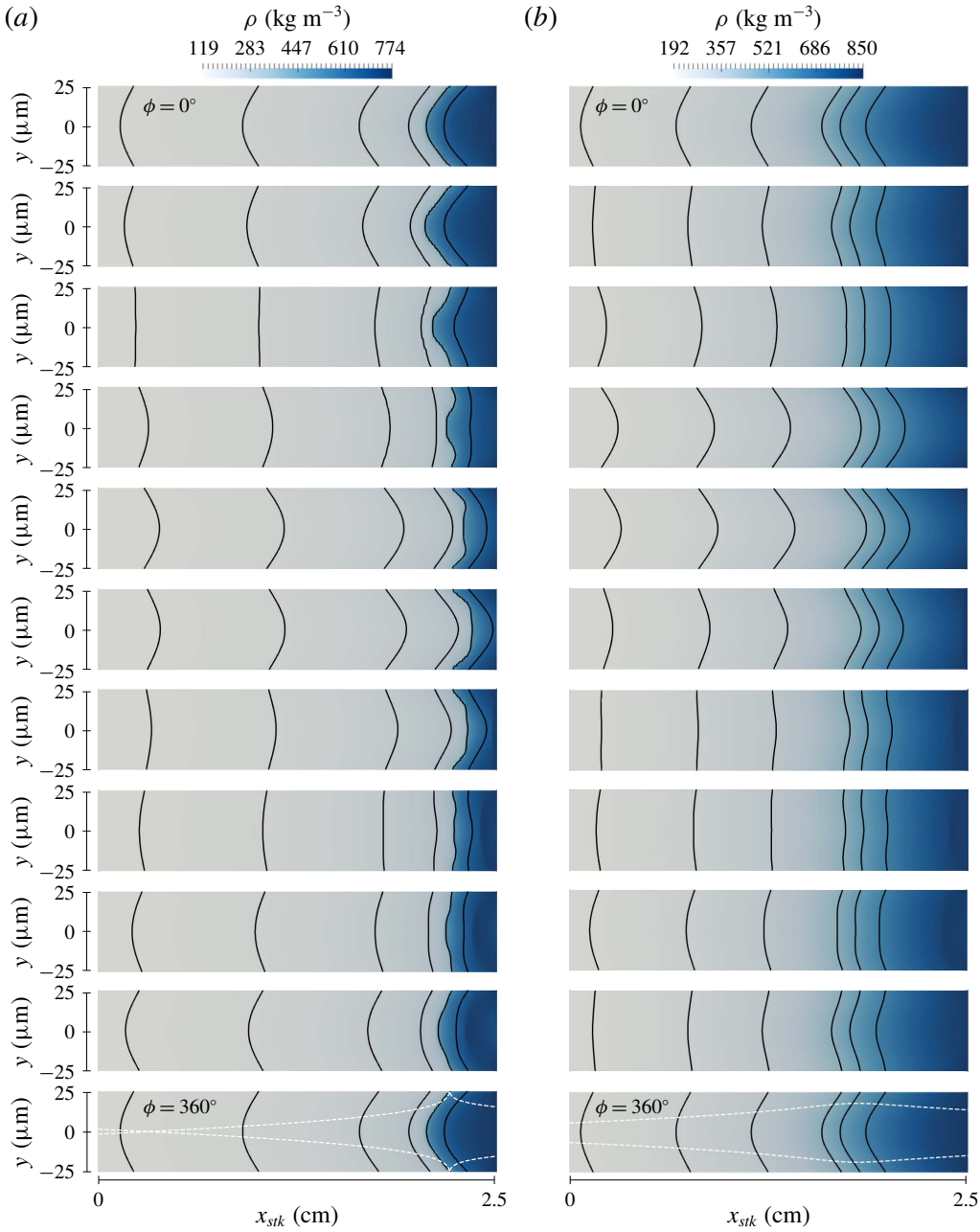

FIGURE 16. Colour contours of density inside the stack for $\Delta T = 100$ K, for $p_0/p_{cr} = 1.01$ (*a*) and $p_0/p_{cr} = 1.5$ (*b*) (see table 2), employing grid B with $N = 3$ (see table 4). A complete acoustic cycle is displayed top to bottom. The results are mirrored about the centre line and stretched 100 times along the y axis for plotting purposes. Solid lines indicate isocontours of density for $\rho = 125, 150, 200, 260, 446.671, 650$ kg m^{-3} (*a*) and $\rho = 200, 240, 300, 450, 521.197, 620$ kg m^{-3} (*b*), while dashed white lines display the local δ_k (see (5.1)). The density oscillations shown correspond to pressure oscillations of approximately 1 % of the base pressure for both (*a*) and (*b*).

of the acoustic cycle, the PB density contour ($\rho = 446.671$ kg m^{-3}) is skewed towards the left, where fluid in PG conditions is present, while it does not extend as much towards the right, halfway through the acoustic cycle, where the PL fluid is. Moreover, the phasing between PG density oscillations ($\rho = 260$ kg m^{-3}) and PL ones ($\rho = 650$ kg m^{-3}) is similar, whereas the PB fluid lags behind, especially in the centre of the channel. In fact, when critical conditions are achieved near the centre of the pore, the thermodynamic properties show a rather flat transverse distribution (figure 17*a*,*c*), due to the high spike in thermal capacity. The thermal inertia is responsible for the increased residence time of the fluid around PB conditions, and contributes to its nonlinear time phasing difference with respect to the oscillations of PG and PL fluid.

On the other hand, for $p_0/p_{cr} = 1.5$ (figure 16*b*), which is sufficiently far from the critical pressure, the stability dynamics is more akin to the ones of ideal gases: away from strong base density gradients, the fluid in the stack undergoes mild and symmetric density oscillations, all with approximately the same relative phasing. Moreover, the acoustic time scale is comparable to the time of thermal diffusion in the y direction, hence allowing for harmonic density perturbations in all the stack.

In fact, the peculiar behaviour of transcritical fluids is connected to the axial profiles of the viscous and thermal boundary layers thicknesses δ_ν, δ_k, defined by

$$\delta_\nu^2 = \frac{2\nu_0}{\omega}, \quad \delta_k^2 = \frac{2k_0}{\omega\rho_0 c_{p_0}} = \frac{\delta_\nu^2}{Pr_0}. \tag{5.1a,b}$$

Since the viscous boundary layer thickness, even for $p_0/p_{cr} = 1.01$, covers most of the fluid inside the stack in all its regions, the cross-sectional velocity profiles resemble their linear counterparts (predicted by the theory of Rott), and do not show significant changes among the different fluid conditions (figure 17*b*). Real-fluid effects are mainly manifest in the oscillating thermodynamic variables, such as density and temperature, but not in the velocity. Indeed, while for gases the Prandtl number is commonly less than unity, and for liquids usually $Pr > 1$, in the PB region the Prandtl number can reach values of 100 (see figure 13*a*). This leads to such a low ratio of thermal boundary layer thickness to half-height of the pore, δ_k/r, that most of the fluid in the pore cannot be heated or cooled by the walls during an acoustic cycle (bottom of figure 16*a*). Therefore, fluid in PB conditions is thermally shielded, and shows large variations and asymmetric characteristics in the transverse profiles of density (figure 17*c*).

The fluid ejection around PB conditions confirms the presence of convective nonlinearities, and suggests that the modal assumption of linear fluctuations is locally violated due to the large changes in particle volume. Indeed, as a result of the PB thermodynamics, the linear relation between density and temperature (A 22), which holds for small wave amplitudes, is replaced by a fully nonlinear relationship even at moderate pressure amplitudes, resulting in a distortion of the Lagrangian pressure–volume cycle (figure 17*d*). However, away from the PB region (and also for higher values of p_0 away from p_{cr}), a pv cycle typical of the linear regime (figure 12) is observed (plot on the left of figure 17*d*). Moreover, pressure oscillation amplitudes, for all values of p_0/p_{cr}, still grow at approximately the rate predicted by the linear theory even with the presence of the aforementioned convective nonlinearities.

In summary, oscillations of transcritical fluids with $p_0/p_{cr} \simeq 1$ present a nonlinear behaviour localized in the small region of the stack where PB conditions are present. However, as discussed in the following section, these nonlinearities are not the ones governing the system's limit cycle.

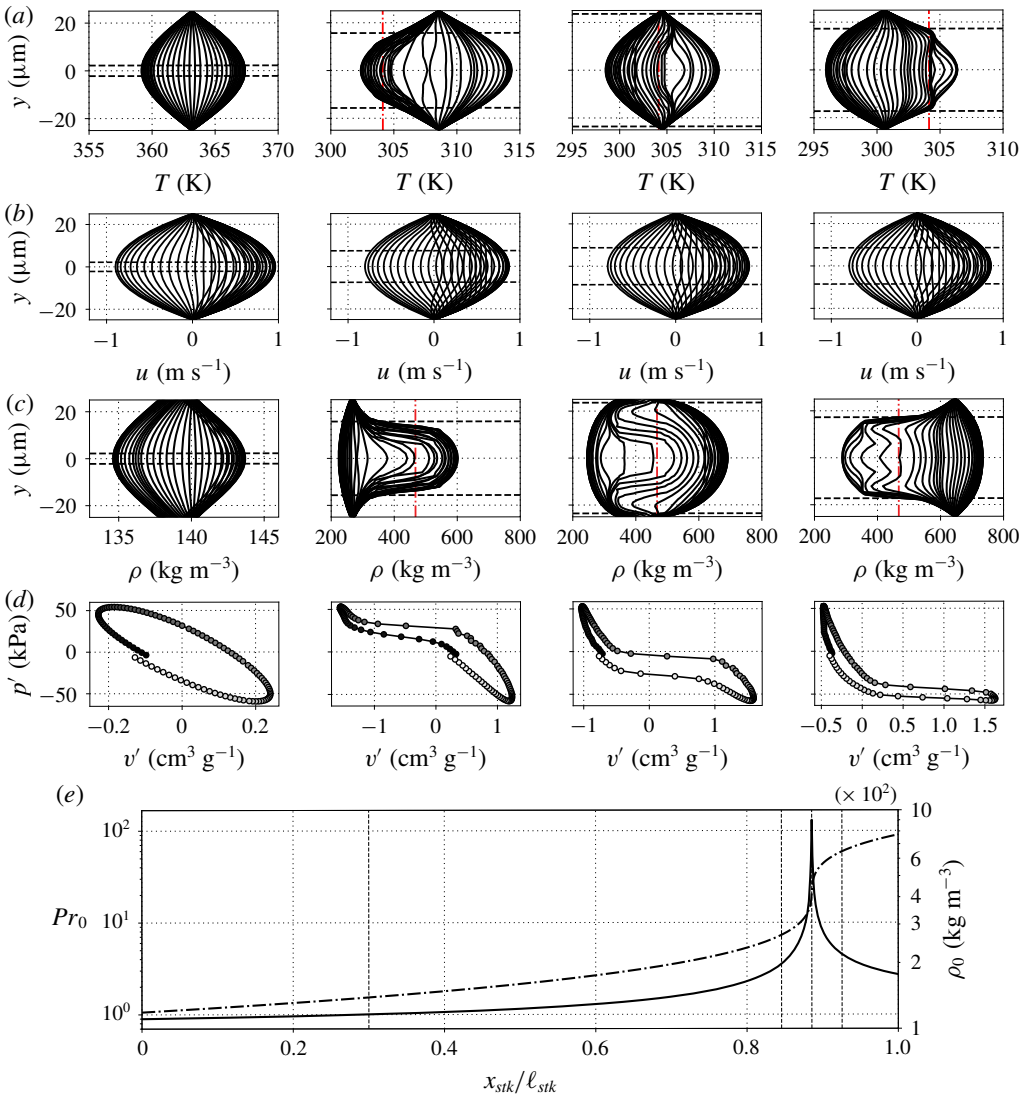

FIGURE 17. Time evolution, during the transient phase, of cross-sectional profiles of temperature (*a*), axial velocity (*b*), and density (*c*) inside the stack, with resulting Lagrangian pressure–volume cycle at the centre line (*d*), for $\Delta T = 100$ K and $p_0/p_{cr} = 1.01$ (see table 1), for grid B with $N = 3$ (see table 4). Darker to lighter coloured circles indicate increasing time in (*d*), which considers a complete acoustic period. The results in (*a*), (*b*), and (*c*), for plotting purposes, are mirrored about the centre line, and are considered until 70 % of the acoustic cycle completion. Horizontal dashed lines indicate the distance from the walls equal to δ_k in (*a*) and (*c*), and to δ_ν in (*b*), and vertical dashed-dotted lines are plotted for $T = T_{cr}$ in (*a*) and for $\rho = \rho_{cr}$ in (*c*). Panel (*e*) shows the base density (dashed-dotted line) and the base Prandtl number (solid line), and vertical dashed lines at $x = 10.75$ cm, 12.11 cm, 12.21 cm, 12.31 cm, which are the axial coordinates from where the *y*-profiles in (*a*), (*b*), (*c*) are extracted from, and the initial locations for the acoustic parcel in (*d*). For this case, the strength of the initial perturbation is $p_{amp} = 5 \times 10^{-3}$ (see (2.9)).

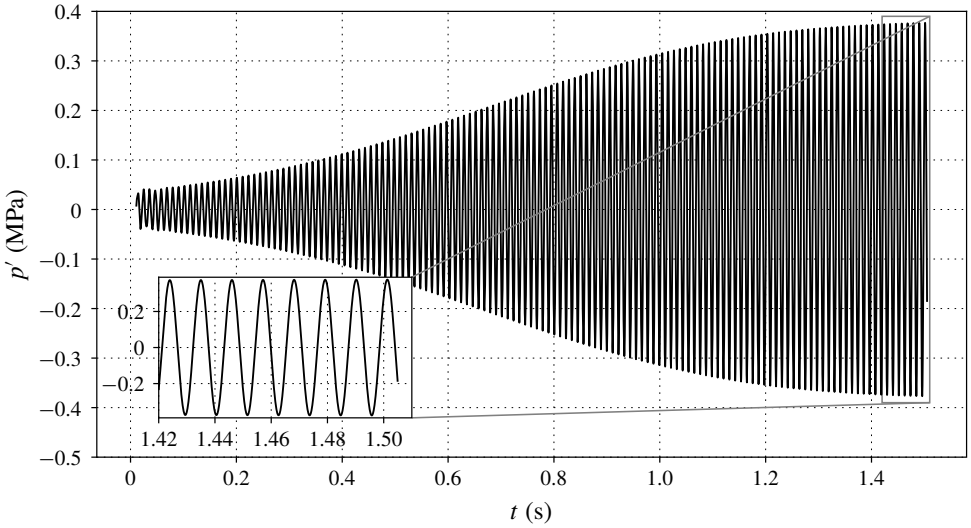

FIGURE 18. Pressure fluctuations detected by a probe at $x = L$ and $y = 0$, for $\Delta T = 30$ K and $p_0 = 1.01 p_{cr}$, from Navier–Stokes simulations with grid A and $N = 2$.

6. Limit cycle due to minor area losses

A limit cycle can be achieved if pressure amplitudes are sufficiently high to trigger nonlinear losses, balancing acoustic energy production via a nonlinear dissipation term, resulting in a zero net energy growth (see (4.3)). One mechanism that can provide high enough nonlinear losses for a limit cycle in a minimal unit calculation is the formation of shock waves (Gupta *et al.* 2017). However, pressurized liquids can sustain large pressure wave amplitudes without the generation of higher harmonics or shock waves. In fact, the pressure amplitude above which acoustic nonlinearities occur, $|p|_{nl}$, which is approximately equal to the reference pressure $\rho_0 a_0^2$ (Migliorino & Scalo 2017), is of the order of hundreds of MPa, corresponding to approximately 15 times the base pressure (table 5), whereas values around 1 %–2 % of p_0 are usually expected for ideal gases. Indeed, Swift (1992) reported the formation of higher harmonics (which indicate incumbent wave steeping) in his experiments on a large-scale ideal-gas thermoacoustic engine, with pressure amplitudes of 10 % of the base pressure, and Gupta *et al.* (2017) showed shock waves at 7 % of the base pressure in their numerical travelling wave set-up with an ideal gas. On the other hand, Migliori & Swift (1988) did not report any trace of higher harmonics at $|p|_{max}/p_0 = 55\,\%$ in their liquid sodium thermoacoustic device, and even proposed a future design for which $|p|_{max}/p_0 = 100\,\%$. The Navier–Stokes simulations carried out in this study from the linear regime to the limit cycle confirm that pressure traces are harmonic (figure 18). A minimal-unit set-up such as the current one will require more acoustic periods to obtain a limit cycle than full scale devices, such as the one investigated by Lin *et al.* (2016), due to its reduced thermoviscous losses. As done in previous studies by Scalo *et al.* (2015), Lin *et al.* (2016) and Gupta *et al.* (2017) a limit cycle is achieved by simulating the complete transient evolution of the system, comprising modal growth and nonlinear saturation, on a coarse grid first. Upon reaching a limit cycle on such grid, the solution is interpolated on progressively finer grids until adequate resolution is reached. On the other hand, when analysing the grid sensitivity analysis of growth rates extracted from the Navier–Stokes simulations,

p_0 (MPa)	7.451	7.746	8.853	10.000	11.066
$\rho_0 a_0^2 \simeq \lvert p\rvert_{nl}$ (MPa)	110.36	114.81	130.52	145.69	159.09
$\lvert p\rvert_{nl}/p_0$	14.81	14.82	14.74	14.57	14.38

TABLE 5. Base pressure, base density times square of base speed of sound, equal to the approximate pressure amplitude limit for nonlinear wave propagation, $|p|_{nl}$, and ratio of $|p|_{nl}$ over base pressure. Data are for all the base pressures of table 2 and for $T = 293.15$ K.

as done in figure 6, all available grid resolutions are adopted from the beginning, and simulations are halted after approximately 8–30 cycles. In no case the complete evolution of the system, from initial conditions to a limit cycle, is simulated on the finest grid available, nor it is advisable to do so.

In the computational set-up considered in this study, the main source of nonlinear dissipation is the vortex shedding at locations of sudden area change, which are the transition from the hot cavity to the stack and from the latter to the duct on its right (see figure 3). Such area jumps entail pressure drops, or minor losses, which can be parametrized as (Idelchik 2003; Lin *et al.* 2016)

$$\Delta\hat{p}_{ml} = -\frac{K}{2}\rho_0 \frac{\hat{U}|\hat{U}|_{lc}}{A_0^2}, \tag{6.1}$$

where $|\hat{U}|/A_0$ is the largest average velocity in the channel and K is defined by

$$K = K_{exp}(A_0/A_1, Re) + K_{contr}(A_0/A_1, Re), \tag{6.2}$$

where A_0 is the smaller and A_1 the larger area. Equation (6.2) considers losses in steady flow due to expansions together with losses from contractions, both dependent, as indicated in Idelchik (2003), on the Reynolds number

$$Re = \frac{\rho_0 h|\hat{U}|_{lc}/A_0}{\mu_0}, \tag{6.3}$$

where h is the height of the stack (see figure 3). The values of $|\hat{U}|$ at limit cycle, $|\hat{U}|_{lc}$, which are different for each area jump, are computed iteratively until a zero growth rate is obtained from the numerical solution of (2.10*a*) and (2.10*b*).

The linear stability theory augmented with linearized minor losses is able to correctly reproduce the axial profiles obtained from the fully nonlinear Navier–Stokes simulations (figure 19*a*,*b*), as was also shown by Lin *et al.* (2016). With respect to the linear regime, (figure 9), the pressure amplitude minimum is null (since $\alpha/\omega = 0$ at limit cycle) and the mass flow rate inside the stack varies more steeply at PB conditions, but the overall axial profiles of pressure amplitude and mass flow rate do not vary considerably. Instead, at limit cycle, the phasing between pressure and flow rate is uniform in the entire resonator, apart from a sharp variation from 90° to −90° (figure 19*c*).

Equations (6.1) and (6.2), by taking into account transitional and fully developed turbulence, are necessary for the quantitative prediction of realistic limit cycle thermoacoustic oscillations (figure 20), which is not obtainable with the two-dimensional Navier–Stokes simulations.

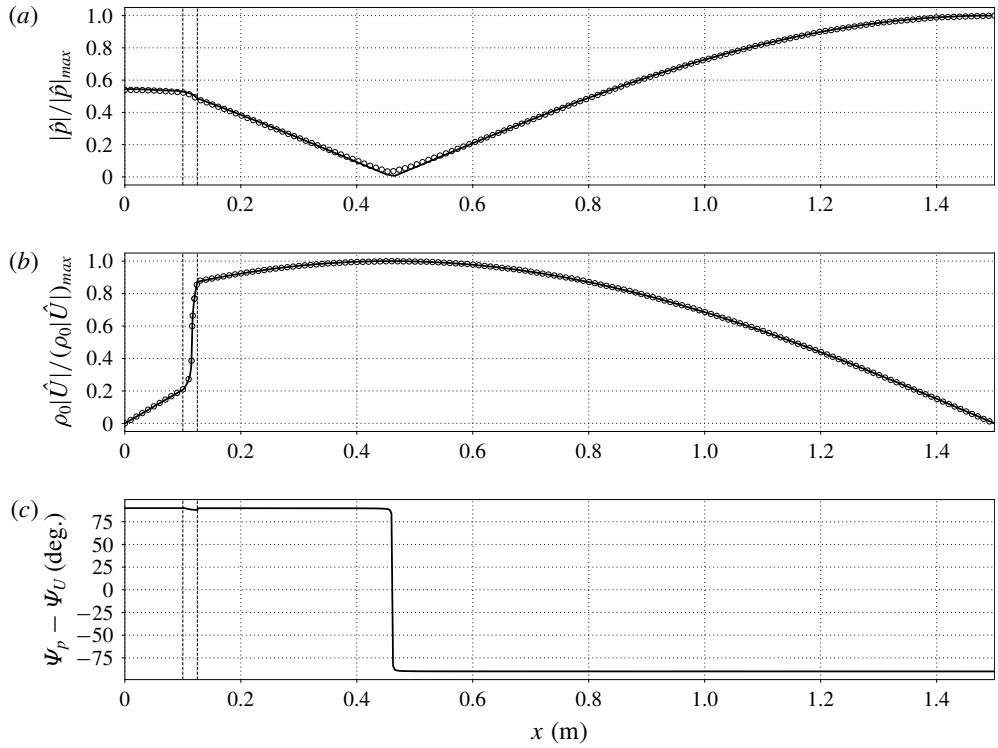

FIGURE 19. Axial distribution of pressure (*a*) and mass flow rate (*b*) dimensionless amplitudes, and phasing between $\hat{p}$ and $\hat{U}$ (*c*), for $\Delta T = 30$ K and $p_0 = 1.01 p_{cr}$, for grid A with $N = 3$ (see table 4), at limit cycle: linear theory augmented with linearized minor losses (solid lines), data extracted from the Navier–Stokes simulations (circles). Vertical dashed lines indicate locations of abrupt area change.

Pressure amplitudes are the highest for near-critical conditions only for values of ΔT below 50 K (figure 20*a*). Furthermore, for a fixed pressure amplitude, conditions away from the critical point are characterized by the lowest Reynolds numbers (figure 20*c*) and work output (figure 20*d*), consistent with that observed in the linear regime (§ 4.1). Thus, as also pointed out by Swift (1988), higher power energy densities are achieved by fluids with larger thermal expansion coefficients, such as fluids with $p_0/p_{cr} \simeq 1$. However, the efficiency of thermal to acoustic energy conversion is the highest for base pressures closer to the critical pressure only if $\Delta T < 30$ K (figure 20*b*), consistent with the theoretical findings of Swift (1988), where higher acoustic powers were associated with lower efficiencies. The maximum efficiency observed is $\eta = 0.87\,\%$, obtained for $p_0/p_{cr} = 1.5$ and $\Delta T = 119$ K. For the sake of comparison, Migliori & Swift (1988), with their liquid sodium thermoacoustic engine, obtained 18 W of acoustic power, employing a 360 K temperature difference across the stack with 990 W of required heat, for an efficiency of 1.8 %. Notice that the computational set-up used in this work was not originally optimized for thermal-to-acoustic efficiency, but for growth rate instead (see § 2.2.2).

The nonlinear behaviour exhibited by the pressure amplitude trends for $\Delta T < 40$ K (see inset in figure 20*a*), which correspond to Reynolds numbers below 10^4, are due to the trends of K_{exp} and K_{contr} appearing in (6.2) (figure 20*e*,*f*). For large Reynolds

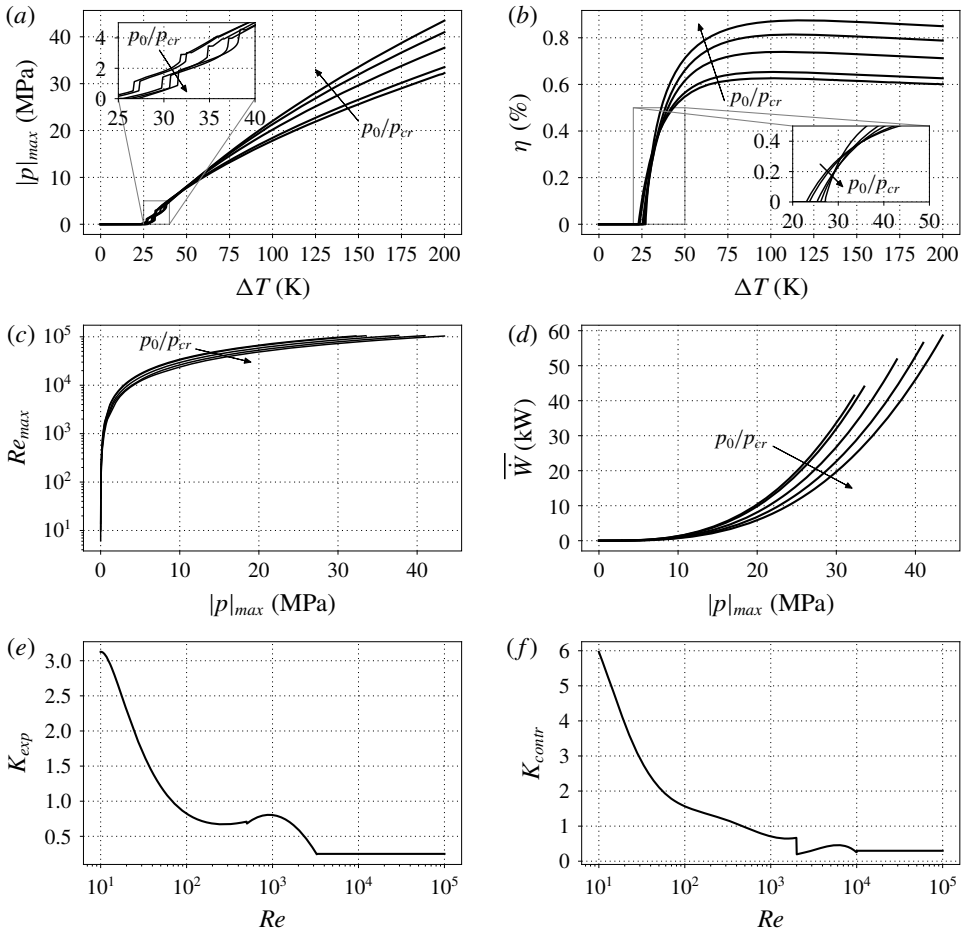

FIGURE 20. Data on limit cycle achieved due to linearized area losses (6.1) for all base pressures of table 2: (*a*) maximum pressure amplitude; (*b*) thermal-to-acoustic efficiency (4.22); (*c*) Reynolds number (6.3); (*d*) acoustic power produced by the stack; (*e*,*f*) K_{exp}, K_{contr} appearing in (6.2) versus Reynolds number for $A_0/A_1 = 0.5$ (Idelchik 2003).

numbers, equation (6.2) becomes (Idelchik 2003)

$$K_{exp} = \left(1 - \frac{A_0}{A_1}\right)^2 \quad \text{for } Re > 3.3 \times 10^3, \quad K_{contr} = \frac{1}{2}\left(1 - \frac{A_0}{A_1}\right)^{3/4} \quad \text{for } Re > 10^4, \tag{6.4a,b}$$

where the first expression is the Borda–Carnot formula. For more accurate predictions of the limit cycle physics, it is recommended that an accurate parametrization for K, i.e. accounting for oscillatory flow, is obtained.

7. Conclusions

This work has unveiled the fundamental physics of transcritical thermoacoustics through the first direct numerical simulation of a thermoacoustically unstable resonator

employing carbon dioxide in transcritical conditions. The main takeaways of this manuscript are the strong real-fluid effects observed in the linear and nonlinear regimes, which are, more specifically as follows:

(i) The high value of the growth rate to frequency ratio (α/ω) which requires, unlike the ideal gas cases, the thermoviscous functions in the linear theory formulation to be based on the fully complex eigenvalue $\alpha + \mathrm{i}\omega$, rather than just its imaginary part ω.

(ii) When the fluid inside the stack approaches pseudo-boiling conditions, the frequency of oscillations drops steeply with small changes in ΔT, with the growth rate exhibiting a non-monotonic dependency with respect to the base pressure p_0.

(iii) A more prominent travelling-wave component than that found in ideal-gas systems in similar configurations is observed at the location of minimum pressure amplitude.

(iv) Due to the steeply varying acoustic impedance, pressure, mass flow rate, and acoustic power exhibit a discontinuity in their first spatial derivative at pseudo-boiling conditions.

(v) The acoustic energy budgets indicate a boost in thermoacoustic production at transcritical conditions, together with a sharp increase in thermoacoustic dissipation; also, the profiles of acoustic power and total energy flux inside the stack suggest that conditions closer to the critical point produce additional power but require more heat input to be sustained.

(vi) Moderate pressure amplitude values (of approximately $1\,\%\,p_0$) trigger thermodynamic nonlinearities, resulting in a highly distorted pressure–volume work cycle, due to the gradients in the base state profiles typical of transcritical fluids with $p_0 \simeq p_{cr}$. However, these nonlinearities are found to be localized in a small region of the stack, and are not responsible for regulating the limit cycle, which is dominated by minor losses at the area jump locations. Axial profiles obtained from the Navier–Stokes simulations pushed to limit cycle are well reproduced by the linear stability theory augmented with linearized minor losses. For this standing-wave configuration, a prediction of the maximum efficiency of thermal to acoustic energy conversion is $0.87\,\%$ at $p_0/p_{cr} = 1.5$ and $\Delta T = 119$ K. Limit cycle work output is found to be always higher for near-critical conditions.

The findings of this work could be helpful for future theoretical and experimental studies on transcritical thermoacoustic instabilities. Future work needs to consider three-dimensional Navier–Stokes simulations for the accurate prediction of the limit cycle physics. Such investigation could shed light on the modelling strategy needed for the pressure drop located at abrupt area jumps, and on the importance of the convective nonlinearities occurring around transcritical conditions. In addition, the effect of bulk viscosity and of gravity needs to be assessed. Moreover, linear stability tools able to consider the steady state energy balance in the stack, with companion conjugate heat transfer Navier–Stokes simulations, need to be considered in the case of transcritical fluids. Finally, more realistic geometrical configurations, such as geometries comprising more than one minimal unit, are desirable.

Acknowledgements

M.T.M. acknowledges the support of the F. N. Andrews and Rolls-Royce Doctoral Fellowships at Purdue University. The use of the SD solver originally developed

by Antony Jameson's group at Stanford University is gratefully acknowledged. The computing resources were provided by the Rosen Center for Advanced Computing (RCAC) at Purdue University and Information Technology at Purdue (ITaP). This work was performed under financial support of the Rolls-Royce University Technology Center at Purdue University, grant number 8000-00198451.

Appendix A. Derivation of the harmonic equations

The evolution equations for mass, axial momentum, and pressure ((2.5), (2.6) and (2.7), respectively), in a two-dimensional domain, with x ($j=1$) corresponding to the axial direction and r ($j=2$) to the radial direction, read

$$\frac{\partial \rho}{\partial t}+u_j\frac{\partial \rho}{\partial x_j}=-\rho\left(\frac{\partial u}{\partial x}+\frac{1}{r^m}\frac{\partial r^m v}{\partial r}\right), \tag{A 1}$$

$$\rho\left(\frac{\partial u}{\partial t}+u_j\frac{\partial u}{\partial x_j}\right)=-\frac{\partial p}{\partial x}+\frac{\mu}{r^m}\frac{\partial}{\partial r}\left(r^m\frac{\partial u}{\partial r}\right), \tag{A 2}$$

$$\frac{\partial p}{\partial t}+u\frac{\partial p}{\partial x}=a^2\left(\frac{\partial \rho}{\partial t}+u_j\frac{\partial \rho}{\partial x_j}\right)+\frac{\alpha_p a^2}{c_p}\left(\tau_{ij}\frac{\partial u_i}{\partial x_j}+\frac{k}{r^m}\frac{\partial}{\partial r}\left(r^m\frac{\partial T}{\partial r}\right)\right), \tag{A 3}$$

where we considered Cartesian ($m=0$) or cylindrical ($m=1$) coordinates, neglected axial viscous and conduction stresses, assumed that $\mu=\mu(x)$ and $k=k(x)$, and disregarded the momentum equation in the r direction ($\partial p/\partial r=0$, $v=v(r)$ and negligible viscous stresses along r).

A first-order Taylor expansion is assumed, both for thermodynamic and kinematic variables,

$$\left.\begin{array}{lll}\rho=\rho_0(x)+\rho'(x,y,t), & T=T_0(x)+T'(x,y,t), & p=p_0+p'(x,t),\\ & u=u'(x,y,t), \quad v=v'(y), & \end{array}\right\} \tag{A 4}$$

where a generic variable is composed of a base quantity, at most varying axially, a fluctuation that is time and space dependent, and no mean flow is considered. Neglecting nonlinear terms, and with the assumptions in (A 4), equation (A 2) becomes

$$\frac{\partial \rho'}{\partial t}+u'\frac{\mathrm{d}\rho_0}{\mathrm{d}x}=-\rho_0\left(\frac{\partial u'}{\partial x}+\frac{1}{r^m}\frac{\partial r^m v'}{\partial r}\right), \tag{A 5}$$

$$\rho_0\frac{\partial u'}{\partial t}=-\frac{\partial p'}{\partial x}+\frac{\mu_0}{r^m}\frac{\partial}{\partial r}\left(r^m\frac{\partial u'}{\partial r}\right), \tag{A 6}$$

$$\frac{\partial p'}{\partial t}=a_0^2\left(\frac{\partial \rho'}{\partial t}+u'\frac{\mathrm{d}\rho_0}{\mathrm{d}x}\right)+\frac{\gamma_0-1}{\alpha_{p_0}T_0}\frac{k_0}{r^m}\frac{\partial}{\partial r}\left(r^m\frac{\partial T'}{\partial r}\right), \tag{A 7}$$

where we used the thermodynamic relation $a^2T\alpha_p^2/c_p=\gamma-1$.

Introducing the variables

$$U'=\int_{-\delta_{0m}h/2}^{h/2}u'(x,r,t)(2\pi r)^m\,\mathrm{d}r,\quad A=\int_{-\delta_{0m}h/2}^{h/2}(2\pi r)^m\,\mathrm{d}r, \tag{A 8a,b}$$

which are, respectively, the volumetric flow rate fluctuations and the cross-sectional area for cylindrical coordinates ($m=1$), or pore height times 1 m for rectilinear

coordinates ($m=0$), and integrating (A 6) over the cross-section, we obtain

$$\rho_0 \frac{\partial U'}{\partial t} = -A \frac{\partial p'}{\partial x} + \tau_w', \quad A \frac{\partial p'}{\partial t} = -\rho_0 a_0^2 \frac{\partial U'}{\partial x} + \frac{\gamma_0 - 1}{\alpha_{p_0} T_0} q', \tag{A 9a,b}$$

after accounting for impenetrable boundary conditions in r, and assuming symmetry of the fluctuations around the centre line of the duct in the expressions of the wall shear stress and the wall heat flux, respectively,

$$\tau_w' = 2\mu_0 \left(\frac{\pi h}{2}\right)^m \left.\frac{\partial u'}{\partial r}\right|_{r=h/2}, \quad q' = 2k_0 \left(\frac{\pi h}{2}\right)^m \left.\frac{\partial T'}{\partial r}\right|_{r=h/2}. \tag{A 10a,b}$$

Assuming an harmonic dependence of the perturbations (normal mode assumption),

$$\left.\begin{aligned} \rho' = \hat{\rho}(x, r)\mathrm{e}^{\sigma t}, \quad T' = \hat{T}(x, r)\mathrm{e}^{\sigma t}, \quad p' = \hat{p}(x)\mathrm{e}^{\sigma t}, \\ u' = \hat{u}(x, r)\mathrm{e}^{\sigma t}, \quad v' = \hat{v}(r)\mathrm{e}^{\sigma t}, \end{aligned}\right\} \tag{A 11}$$

where it is intended that the physical solution of all the perturbations is the real part of the respective expressions, equation (A 6) becomes

$$\sigma \hat{\rho} = -\rho_0 \frac{\partial \hat{u}}{\partial x} - \hat{u} \frac{\mathrm{d}\rho_0}{\mathrm{d}x} - \frac{\rho_0}{r^m} \frac{\partial r^m \hat{v}}{\partial r}, \tag{A 12}$$

$$\sigma \hat{u} = -\frac{1}{\rho_0} \frac{\mathrm{d}\hat{p}}{\mathrm{d}x} + \frac{\nu_0}{r^m} \frac{\partial}{\partial r}\left(r^m \frac{\partial \hat{u}}{\partial r}\right), \tag{A 13}$$

$$\sigma \left(\hat{\rho} - \frac{1}{a_0^2}\hat{p}\right) = -\hat{u} \frac{\mathrm{d}\rho_0}{\mathrm{d}x} + \frac{\nu_0}{Pr_0} \frac{1}{r^m} \frac{\partial}{\partial r}\left(r^m \frac{\partial \hat{\rho}}{\partial r}\right), \tag{A 14}$$

which are the harmonic mass, momentum, pressure equations and the frequency-domain expression of (A 9) reads

$$\rho_0 \sigma \hat{U} = -A \frac{\mathrm{d}\hat{p}}{\mathrm{d}x} + \hat{\tau}_w, \quad A\sigma \hat{p} = -\rho_0 a_0^2 \frac{\partial \hat{U}}{\partial x} + \frac{\gamma_0 - 1}{\alpha_{p_0} T_0} \hat{q}. \tag{A 15a,b}$$

Despite not having made any assumption on the fluid, equation (A 13) coincides with the equations proposed by Rott (1969), who used the ideal gas EoS.

The coordinate transformation

$$\xi = \mathrm{i}\eta, \quad \eta = \sqrt{\frac{\sigma}{\nu_0}} r = \sqrt{2\mathrm{i} + 2\frac{\alpha}{\omega}} \frac{r}{\delta_\nu}, \tag{A 16a,b}$$

which is a generalization of the case $\alpha \ll \omega$ ($\sigma \approx \mathrm{i}\omega$) (Rott 1969; Swift *et al.* 1985; Lin *et al.* 2016; Gupta *et al.* 2017), for which $\eta = \sqrt{2\mathrm{i}} r/\delta_\nu = (\mathrm{i}+1) r/\delta_\nu$, allows us to rewrite the harmonic momentum equation as

$$\xi^2 \frac{\partial^2 \widehat{u}_*}{\partial \xi^2} + m\xi \frac{\partial \widehat{u}_*}{\partial \xi} + \xi^2 \widehat{u}_* = 0, \tag{A 17}$$

where $\widehat{u}_* = -\sigma\rho_0 \hat{u}/(\mathrm{d}\hat{p}/\mathrm{d}x) - 1$. Equation (A 17), in the case of $m=1$, is a Bessel's differential equation of order 0. Equation (A 17) has the general solution

$$(m=1): \quad \widehat{u}_*(\xi) = -\frac{\mathrm{J}_0(\xi)}{\mathrm{J}_0(\xi_b)}, \quad (m=0): \quad \widehat{u}_*(\eta) = -\frac{\cosh(\eta)}{\cosh(\eta_b)}, \tag{A 18a,b}$$

where J_0 is the Bessel function of the first kind of order 0, the subscript b indicates evaluation at $r=h/2$, i.e. $\eta_b=\sqrt{\sigma/\nu_0}h/2$, and the no-slip boundary condition has been taken into account ($\widehat{u}_*(\xi_b)=\widehat{u}_*(\eta_b)=-1$). Therefore the solution of the momentum equation and the wall shear stress in frequency domain are

$$\hat{u}=-\frac{1}{\sigma\rho_0}\frac{\mathrm{d}\hat{p}}{\mathrm{d}x}(\widehat{u}_*+1),\quad \hat{\tau}_w=A\frac{\mathrm{d}\hat{p}}{\mathrm{d}x}f_v, \tag{A 19a,b}$$

and the first of (A 15) is

$$\sigma\hat{U}=-\frac{A}{\rho_0}\frac{\mathrm{d}\hat{p}}{\mathrm{d}x}(1-f_v), \tag{A 20}$$

where

$$(m=1):\quad f_v=\frac{2}{\xi_b}\frac{J_1(\xi_b)}{J_0(\xi_b)},\quad (m=0):\quad f_v=\frac{\tanh(\eta_b)}{\eta_b}. \tag{A 21a,b}$$

The linearized harmonic EoS,

$$\gamma_0\frac{\hat{p}}{\rho_0{a_0}^2}=\frac{\hat{\rho}}{\rho_0}+\alpha_{p_0}\hat{T}, \tag{A 22}$$

evaluated at the walls, where isothermal boundary conditions ($\hat{T}_w=0$) are applied, becomes

$$\hat{\rho}_w=\frac{\gamma_0}{{a_0}^2}\hat{p}, \tag{A 23}$$

where we used the independency of $\hat{p}$ from r. Using (A 16), the harmonic pressure equation becomes

$$\frac{\partial^2}{\partial\xi^2}(\hat{\rho}-\hat{\rho}_w)+\frac{m}{\xi}\frac{\partial}{\partial\xi}(\hat{\rho}-\hat{\rho}_w)+Pr_0(\hat{\rho}-\hat{\rho}_w)=-Pr_0\frac{\gamma_0-1}{{a_0}^2}\hat{p}-\frac{Pr_0}{\sigma}\hat{u}\frac{\mathrm{d}\rho_0}{\mathrm{d}x}, \tag{A 24}$$

that is the inhomogeneous analogue of (A 17). To revert back to an homogeneous equation, we assume a solution of the form

$$(\hat{\rho}-\hat{\rho}_w)=\frac{\rho_0\Theta}{\sigma}\frac{Pr_0}{1-Pr_0}\hat{u}(\xi)+(\rho-\hat{\rho}_w)_2, \tag{A 25}$$

where we assumed $Pr_0\neq 1$ everywhere axially, obtaining from (A 24) the equation

$$\left.\begin{aligned}&\tilde{\xi}^2\frac{\partial^2\widehat{\rho}_*}{\partial\tilde{\xi}^2}+m\tilde{\xi}\frac{\partial\widehat{\rho}_*}{\partial\tilde{\xi}}+\tilde{\xi}^2\widehat{\rho}_*=0,\quad \tilde{\xi}=\xi\sqrt{Pr_0},\\ &\widehat{\rho}_*=-(\hat{\rho}-\hat{\rho}_w)_2\left(\frac{\gamma_0-1}{{a_0}^2}\hat{p}+\frac{\Theta}{(1-Pr_0)\sigma^2}\frac{\mathrm{d}\hat{p}}{\mathrm{d}x}\right)^{-1}-1,\end{aligned}\right\} \tag{A 26}$$

which can be solved with a solution of the form of (A 18) replacing ξ with $\tilde{\xi}$, taking advantage of the wall boundary conditions,

$$(m=1):\quad \widehat{\rho}_*(\xi)=-\frac{J_0(\xi\sqrt{Pr_0})}{J_0(\xi_b\sqrt{Pr_0})},\quad (m=0):\quad \widehat{\rho}_*(\eta)=-\frac{\cosh(\eta\sqrt{Pr_0})}{\cosh(\eta_b\sqrt{Pr_0})}. \tag{A 27a,b}$$

We can therefore write the harmonic density equation as follows:

$$\hat{\rho} - \hat{\rho}_w = -(\mathcal{R} + \hat{p}(\gamma_0 - 1)/{a_0}^2)(\widehat{\rho}_* + 1) + \mathcal{R}Pr_0(\widehat{u}_* + 1), \tag{A 28}$$

where

$$\mathcal{R} = \frac{\Theta/\sigma^2}{1 - Pr_0}\frac{\mathrm{d}\hat{p}}{\mathrm{d}x}. \tag{A 29}$$

Here, as noticed before, the derivation of Rott, performed under the assumption of ideal gases, still holds for a generic fluid, in the case of $Pr_0 \neq 1$.

We can now evaluate the wall heat flux in the frequency domain,

$$\hat{q} = \sigma A \frac{c_{p_0}}{\alpha_{p_0}}\left(-\frac{\Theta}{(1 - Pr_0)\sigma^2}\frac{\mathrm{d}\hat{p}}{\mathrm{d}x}(f_k - f_\nu) - \frac{\gamma_0 - 1}{a_0^2}\hat{p}f_k\right), \tag{A 30}$$

where the term $1/\alpha_{p_0}$ reverts back to T_0 in the case of ideal gas EoS (Gupta *et al.* 2017), and where

$$(m = 1):\quad f_k = \frac{2}{\xi_b\sqrt{Pr_0}}\frac{\mathrm{J}_1(\xi_b\sqrt{Pr_0})}{\mathrm{J}_0(\xi_b\sqrt{Pr_0})},\qquad (m = 0):\quad f_k = \frac{\tanh(\eta_b\sqrt{Pr_0})}{\eta_b\sqrt{Pr_0}}. \tag{A 31a,b}$$

Equations (A 21) and (A 31) define the thermoviscous functions.

Finally, the pressure equation in harmonic form can be written as

$$\sigma\hat{p} = \frac{\rho_0 a_0^2/A}{1 + (\gamma_0 - 1)f_k}\left(\frac{\Theta(f_k - f_\nu)}{(1 - f_\nu)(1 - Pr_0)} - \frac{\mathrm{d}}{\mathrm{d}x}\right)\hat{U}. \tag{A 32}$$

Appendix B. Discussion of minimum pressure amplitude

Expressing $\hat{p}$ and $\hat{U}$ in the conventional complex phasor notation, $\hat{p} = |\hat{p}|\mathrm{e}^{\mathrm{i}\Psi_p}$ and $\hat{U} = |\hat{U}|\mathrm{e}^{\mathrm{i}\Psi_U}$ in (2.10*a*) yields

$$\hat{U} = -\frac{A}{\sigma\rho_0 F_\nu}\mathrm{e}^{\mathrm{i}\Psi_p}\left(\frac{\mathrm{d}|\hat{p}|}{\mathrm{d}x} + \mathrm{i}|\hat{p}|\frac{\mathrm{d}\Psi_p}{\mathrm{d}x}\right), \tag{B 1}$$

hence

$$|\hat{U}| = \frac{A}{|\sigma|\rho_0|F_\nu|}\sqrt{\left(\frac{\mathrm{d}|\hat{p}|}{\mathrm{d}x}\right)^2 + \left(|\hat{p}|\left|\frac{\mathrm{d}\Psi_p}{\mathrm{d}x}\right|\right)^2}, \tag{B 2}$$

$$\mathrm{e}^{\mathrm{i}(\Psi_U - \Psi_p)} = -\frac{|\sigma||F_\nu|}{\sigma F_\nu}\left(\frac{\mathrm{d}|\hat{p}|}{\mathrm{d}x} + \mathrm{i}|\hat{p}|\frac{\mathrm{d}\Psi_p}{\mathrm{d}x}\right)\Big/\sqrt{\left(\frac{\mathrm{d}|\hat{p}|}{\mathrm{d}x}\right)^2 + \left(|\hat{p}|\left|\frac{\mathrm{d}\Psi_p}{\mathrm{d}x}\right|\right)^2}, \tag{B 3}$$

and, from (2.10*b*),

$$\sigma|\hat{p}|\mathrm{e}^{\mathrm{i}(\Psi_p - \Psi_u)}\frac{AF_k}{\rho_0 a_0^2} = |\hat{U}|\left(\Theta\Phi_{\mathcal{P}} - \mathrm{i}\frac{\mathrm{d}\Psi_U}{\mathrm{d}x}\right) - \frac{\mathrm{d}|\hat{U}|}{\mathrm{d}x}. \tag{B 4}$$

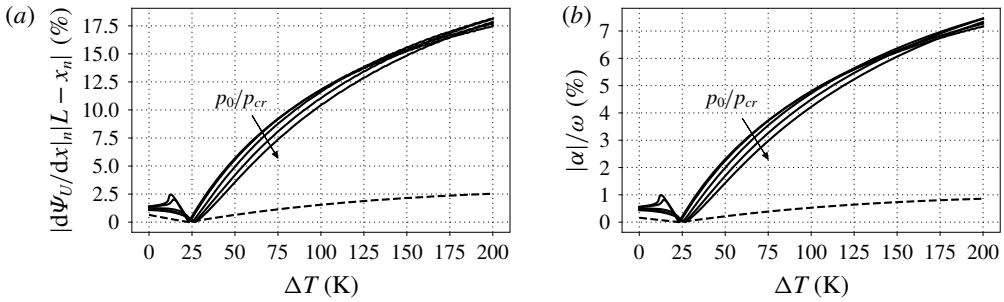

FIGURE 21. Data from linear stability theory: (*a*) product of the absolute value of the phase derivative of flow rate at the minimum pressure amplitude location (x_n) and absolute value of distance of x_n from the right-hand end side of the resonator (term present in the right-hand side of (B 11)); (*b*) ratio of the absolute value of growth rate to angular frequency. Solid lines are for real-fluid EoS (for all base pressures in table 2), and the dashed line indicates ideal gas EoS (for $p_0 = 10$ MPa only).

In the duct on the right of the stack the base state is uniform, hence $\Theta = 0$, and inviscid walls are assumed ($F_\nu = F_k = 1$). There, where the pressure is minimum, if α is not too close to 0, $|\hat{U}|$ can be assumed to be maximum. Therefore, at $x = x_{|p|_{min}} = x_n$, $\mathrm{d}|\hat{p}|/\mathrm{d}x|_n = \mathrm{d}|\hat{U}|/\mathrm{d}x|_n = 0$ in (B 2), (B 3), and (B 4) yields

$$|\hat{U}|_n = \frac{A}{|\sigma|\rho_0}|\hat{p}|_n \left|\frac{\mathrm{d}\Psi_p}{\mathrm{d}x}\right|_n, \tag{B 5}$$

$$\mathrm{e}^{\mathrm{i}(\Psi_{p_n} - \Psi_{U_n})} = \mathrm{i}\frac{\sigma}{|\sigma|}\mathrm{sgn}\left(\left.\frac{\mathrm{d}\Psi_p}{\mathrm{d}x}\right|_n\right) \rightarrow \Psi_{p_n} - \Psi_{U_n} = -\arctan\left(\frac{\alpha}{\omega}\right), \tag{B 6}$$

$$\frac{|\sigma|^2}{a_0^2} = \left|\frac{\mathrm{d}\Psi_p}{\mathrm{d}x}\right|_n \left|\frac{\mathrm{d}\Psi_U}{\mathrm{d}x}\right|_n. \tag{B 7}$$

Equation (B 5) shows that, in order to have maximum $|\hat{U}|_n$, $|\mathrm{d}\Psi_p/\mathrm{d}x|_n$ has to be maximum. Equations (B 5), (B 6) and (B 7) have been verified with the data obtained from the linear theory (not shown).

In § 3.2 it was stated that $|\hat{p}|_{min}/|\hat{p}|_{max}$ (figure 10*b*) is proportional to $|\alpha|/\omega$ (figure 21*b*). This can be explained by noticing that, outside of the stack, equation (4.3) becomes

$$\frac{\mathrm{d}\overline{\dot{W}}}{\mathrm{d}x} = -\alpha\overline{\mathcal{E}}, \tag{B 8}$$

and by assuming an acoustic energy distribution (4.4) equal to its value at $x = L$ (where $|\hat{U}| = 0$). After integrating (B 8) from the right end side of the stack to the right end side of the resonator, the acoustic power at $x = x_n$ is

$$\overline{\dot{W}}_n = |\hat{p}|_n|\hat{U}|_n\left(-\frac{\omega}{|\sigma|}\right)\mathrm{sgn}\left(\left.\frac{\mathrm{d}\Psi_p}{\mathrm{d}x}\right|_n\right) = \frac{\alpha A}{2\rho_0 a_0^2}|\hat{p}|_{max}^2(L - x_n). \tag{B 9}$$

This is consistent with the intuitive reasoning that, if there is growth, nowhere in the resonator the acoustic power flow can be blocked by a stationary node, which would

instead happen for a perfectly standing wave (zero acoustic power), which has $\alpha = 0$. Inserting (B 5) in (B 9) yields

$$\left(\frac{|\hat{p}|_n}{|\hat{p}|_{max}}\right)^2 = -\frac{|\sigma|^2\alpha}{2a_0^2\omega}(L - x_n) \bigg/ \left.\frac{\mathrm{d}\Psi_p}{\mathrm{d}x}\right|_n, \tag{B 10}$$

which proves that, since the left-hand side is always positive, $\alpha/(\mathrm{d}\Psi_p/\mathrm{d}x)|_n \leqslant 0$. Using (B 7) in (B 10), after taking the absolute value of its right-hand side, yields

$$\left(\frac{|\hat{p}|_n}{|\hat{p}|_{max}}\right)^2 = \frac{1}{2}\frac{|\alpha|}{\omega}\left|\frac{\mathrm{d}\Psi_U}{\mathrm{d}x}\right|_n |L - x_n|. \tag{B 11}$$

With the data obtainable from the linear theory, it is found that $|\mathrm{d}\Psi_U/\mathrm{d}x|_n|L - x_n|$ (figure 21*a*) is proportional to $|\alpha|/\omega$ (figure 21*b*), hence also

$$\frac{|\hat{p}|_{min}}{|\hat{p}|_{max}} \propto \frac{|\alpha|}{\omega}, \tag{B 12}$$

explaining the trend observed in figure 10(*b*).

REFERENCES

ABGRALL, R. 1996 How to prevent pressure oscillations in multicomponent flow calculations: a quasi conservative approach. *J. Comput. Phys.* **125** (1), 150–160.

ALEXANDER, D., MIGLIORINO, M. T., HEISTER, S. D. & SCALO, C. 2018 Numerical and experimental analysis of a transcritical thermoacoustic prototype. In *2018 Fluid Dynamics Conference*. American Institute of Aeronautics and Astronautics.

BACKHAUS, S. & SWIFT, G. W. 1999 A thermoacoustic Stirling heat engine. *Nature* **399** (6734), 335–338.

BACKHAUS, S. & SWIFT, G. W. 2000 A thermoacoustic-Stirling heat engine: detailed study. *J. Acoust. Soc. Am.* **107**, 3148–3166.

BANUTI, D. T. 2015 Crossing the Widom-line – supercritical pseudo-boiling. *J. Supercrit. Fluids* **98**, 12–16.

CASIANO, M. J., HULKA, J. R. & YANG, V. 2010 Liquid-propellant rocket engine throttling: a comprehensive review. *J. Propul. Power* **26** (5), 897–923.

CEPERLEY, P. H. 1979 A pistonless Stirling engine – the traveling wave heat engine. *J. Acoust. Soc. Am.* **66**, 1239–1244.

CHUNG, T.-H., AJLAN, M., LEE, L. L. & STARLING, K. E. 1988 Generalized multiparameter correlation for nonpolar and polar fluid transport properties. *Ind. Engng Chem. Res.* **27** (4), 671–679.

ELISON, B. P., MANN, P. V. & SINHA, A. K. 2014 Implementing microscale thermoacoustic heat and power control for processors and 3d chipstacks. US Patent App. 13/624,051.

FAITH, L. E., ACKERMAN, G. H. & HENDERSON, H. T. 1971 Heat sink capability of Jet A fuel: heat transfer and coking studies. *Tech. Rep.* Shell Development Company.

FISHER, M. E. & WIDOM, B. 1969 Decay of correlations in linear systems. *J. Chem. Phys.* **50** (20), 3756–3772.

GUPTA, P., LODATO, G. & SCALO, C. 2017 Spectral energy cascade in thermoacoustic shock waves. *J. Fluid Mech.* **831**, 358–393.

HERRING, N. R. 2007 On the development of compact, high performance heat exchangers for gas turbine applications. PhD thesis, Purdue University.

HERRING, N. R. & HEISTER, S. D. 2006 Review of the development of compact, high performance heat exchangers for gas turbine applications. In *ASME International Mechanical Engineering Congress and Exposition*. ASME.

HINES, W. S. & WOLF, H. 1962 Pressure oscillations associated with heat transfer to hydrocarbon fluids at supercritical pressures and temperatures. *Am. Rocket Soc. J.* **32** (3), 361–366.

HITCH, B. & KARPUK, M. 1998 Enhancement of heat transfer and elimination of flow oscillations in supercritical fuels. In *34th AIAA/ASME/SAE/ASEE Joint Propulsion Conference and Exhibit*. American Institute of Aeronautics and Astronautics.

HUNT, S. 2016 Thermoacoustic oscillations in supercritical fluid flows. PhD thesis, Purdue University.

HUNT, S. & HEISTER, S. D. 2014 Thermoacoustic oscillations in supercritical fuel flows. In *12th International Energy Conversion Engineering Conference*. American Institute of Aeronautics and Astronautics.

IDELCHIK, I. E. 2003 *Handbook of Hydraulic Resistance*, 3rd edn. CRC Press.

KARNI, S. 1994 Multicomponent flow calculations by a consistent primitive algorithm. *J. Comput. Phys.* **112** (1), 31–43.

KAWAI, S., TERASHIMA, H. & NEGISHI, H. 2015 A robust and accurate numerical method for transcritical turbulent flows at supercritical pressure with an arbitrary equation of state. *J. Comput. Phys.* **300** (Supplement C), 116–135.

KIRCHHOFF, G. 1868 Über den Einfluss der Wärmeleitung in einem Gase auf die Schallbewegung. *Pogg. Ann.* **134**, 177–193.

KRAMERS, H. A. 1949 Vibrations of a gas column. *Physica* **15** (971), 971–984.

LIN, J., SCALO, C. & HESSELINK, L. 2016 High-fidelity simulation of a standing-wave thermoacoustic–piezoelectric engine. *J. Fluid Mech.* **808**, 19–60.

LINNE, D., MEYER, M., EDWARDS, T. & EITMAN, D. 1997 Evaluation of heat transfer and thermal stability of supercritical JP-7 fuel. In *33rd Joint Propulsion Conference and Exhibit*. American Institute of Aeronautics and Astronautics.

MALONE, J. F. J. 1931 A new prime mover. *J. R. Soc. Arts* **79** (4099), 679–709.

MIGLIORI, A. & SWIFT, G. W. 1988 Liquid sodium thermoacoustic engine. *Appl. Phys. Lett.* **53** (5), 355–357.

MIGLIORINO, M. T., CHAPELIER, J.-B., SCALO, C. & LODATO, G. 2018 Assessment of spurious numerical oscillations in high-order spectral difference solvers for supercritical flows. In *2018 Fluid Dynamics Conference*. American Institute of Aeronautics and Astronautics.

MIGLIORINO, M. T., GUPTA, P. & SCALO, C. 2017 Real fluid effects on thermoacoustic standing-wave resonance in supercritical CO_2. In *8th AIAA Theoretical Fluid Mechanics Conference*. American Institute of Aeronautics and Astronautics.

MIGLIORINO, M. T. & SCALO, C. 2017 Dimensionless scaling of heat-release-induced planar shock waves in near-critical CO_2. In *55th AIAA Aerospace Sciences Meeting*, American Institute of Aeronautics and Astronautics.

O'NEILL, L. E. & MUDAWAR, I. 2018 Mechanistic model to predict frequency and amplitude of density wave oscillations in vertical upflow boiling. *Intl J. Heat Mass Transfer* **123**, 143–171.

PALUMBO, M. 2009 Predicting the onset of thermoacoustic oscillations in supercritical fluids. Master's thesis, Purdue University, West Lafayette, IN.

PANTANO, C., SAUREL, R. & SCHMITT, T. 2017 An oscillation free shock-capturing method for compressible van der Waals supercritical fluid flows. *J. Comput. Phys.* **335**, 780–811.

PENG, D.-Y. & ROBINSON, D. B. 1976 A new two-constant equation of state. *Ind. Engng Chem. Fundam.* **15** (1), 59–64.

PETACH, M., TWARD, E. & BACKHAUS, S. 2004 Design of a High Efficiency Power Source (HEPS) based on thermoacoustic technology. *NASA Tech. Rep.*

POINSOT, T. & VEYNANTE, D. 2011 *Theoretical and Numerical Combustion*, 3rd edn. R.T. Edwards, Inc.

RAYLEIGH 1878 The explanation of certain acoustical phenomena. *Nature* **18**, 319–321.

ROTT, N. 1969 Damped and thermally driven acoustic oscillations in wide and narrow tubes. *Z. Angew. Math. Phys.* **20**, 230–243.

SCALO, C., LELE, S. K. & HESSELINK, L. 2015 Linear and nonlinear modeling of a theoretical traveling-wave thermoacoustic heat engine. *J. Fluid Mech.* **766**, 368–404.

SOAVE, G. 1972 Equilibrium constants from a modified Redlich–Kwong equation of state. *Chem. Engng Sci.* **27**, 1197–1203.

SWIFT, G. W. 1988 Thermoacoustic engines. *J. Acoust. Soc. Am.* **84** (4), 1145–1181.

SWIFT, G. W. 1992 Analysis and performance of a large thermoacoustic engine. *J. Acoust. Soc. Am.* **92** (3), 1551–1563.

SWIFT, G. W., MIGLIORI, A., HOFLER, T. & WHEATLEY, J. 1985 Theory and calculations for an intrinsically irreversible acoustic prime mover using liquid sodium as primary working fluid. *J. Acoust. Soc. Am.* **78** (2), 767–781.

TIJANI, M. E. H. & SPOELSTRA, S. 2011 A high performance thermoacoustic engine. *J. Appl. Phys.* **110**, 093519.

TORO, E. F. 2002 Anomalies of conservative methods: analysis, numerical evidence and possible cures. *Comput. Fluid Dyn. J.* **11** (1), 128–143.

TUCKER, S. C. 1999 Solvent density inhomogeneities in supercritical fluids. *Chem. Rev.* **99**, 391–418.

WANG, H., ZHOU, J., PAN, Y. & WANG, N. 2015 Experimental investigation on the onset of thermo-acoustic instability of supercritical hydrocarbon fuel flowing in a small-scale channel. *Acta Astron.* **117**, 296–304.

WARD, B., CLARK, J. & SWIFT, G. 2012 *Design Environment for Low-Amplitude Thermoacoustic Energy Conversion: Users Guide*. Los Alamos National Laboratory.

YAZAKI, T., IWATA, A., MAEKAWA, T. & TOMINAGA, A. 1998 Traveling wave thermoacoustic engine in a looped tube. *Phys. Rev. Lett.* **81** (15), 3128–3131.